

1 **Impact of scale-aware deep convection on the cloud liquid and ice water paths and precipitation using the**
2 **Model for Prediction Across Scales (MPAS-v5.2)**

3 **Laura D. Fowler¹, Mary C. Barth¹, and Kiran Alapaty²**

4 ¹National Center for Atmospheric Research, Boulder, Colorado

5 ²Center for Environmental Measurements and Modeling, U.S. Environmental Protection Agency
6 Research Triangle Park, North Carolina

7
8
9 Revised for Geoscientific Model Development
10 April 2020
11
12
13
14
15
16
17
18
19
20
21
22
23
24
25
26
27
28
29
30
31
32
33
34
35
36
37
38
39
40
41
42
43
44
45
46
47
48

49 *Corresponding author address:* Dr. Laura D. Fowler, National Center for Atmospheric Research. P.O. Box 3000,
50 Boulder, CO 80307-3000, USA.

51 E-mail: laura@ucar.edu

52 **Abstract.** The cloud Liquid Water Path (LWP), Ice Water Path (IWP), and precipitation simulated with uniform-
53 and variable-resolution numerical experiments using the Model for Prediction Across Scales (MPAS) are compared
54 against Clouds and the Earth’s Radiant Energy System (CERES) and Tropical Rainfall Measuring Mission data. Our
55 comparison between monthly mean model diagnostics and satellite data focuses on the convective activity regions of
56 the Tropical Pacific Ocean, extending from the Eastern Tropical Pacific Basin where trade wind boundary layer clouds
57 develop to the Western Pacific warm pool characterized by deep convective updrafts capped with extended upper-
58 tropospheric ice clouds. Using the scale-aware Grell-Freitas (GF) and Multi-Scale Kain-Fritsch (MSKF) convection
59 schemes in conjunction with the Thompson cloud microphysics, uniform-resolution experiments produce large biases
60 between simulated and satellite-retrieved LWP, IWP, and precipitation. Differences in the treatment of shallow
61 convection lead the LWP to be strongly overestimated when using GF while being in relatively good agreement when
62 using MSKF compared to CERES data. Over areas of deep convection, uniform- and variable-resolution experiments
63 overestimate the IWP with both MSKF and GF, leading to strong biases in the top-of-the-atmosphere long- and short-
64 wave radiation relative to satellite-retrieved data. Mesh refinement over the Western Pacific warm pool does not lead
65 to significant improvement in the LWP, IWP, and precipitation due to increased grid-scale condensation and upward
66 vertical motions. Results underscore the importance of evaluating clouds, their optical properties, and the top-of-the-
67 atmosphere radiation budget in addition to precipitation when performing mesh refinement global simulations.

68 **1 Introduction**

69 Comparing simulated against observed global cloud liquid and ice water paths (LWP and IWP) remains challenging
70 because of uncertainties in parameterizing moist processes and cloudiness in global climate and numerical weather
71 prediction (NWP) models, and errors in retrieving the LWP and IWP from satellite measurements. Cloud simulations
72 from general circulation models (GCMs) involved in Phase 3 and 5 of the Coupled Model Intercomparison Project
73 (CMIP3; CMIP5; Meehl et al, 2007; Taylor et al., 2012) display a strong disparity in the simulated LWP (Jiang et al.,
74 2012; Li et al., 2018) and IWP (Li et al., 2012), producing annual mean LWP and IWP overestimated by factors of 2
75 to 10 compared to satellite data. Satellite observations of the LWP and IWP from passive nadir viewing instruments
76 such as the Moderate-resolution Imaging Spectroradiometer (MODIS; Minnis et al., 2011), and profiling radar such
77 as the 94-GHz instrument on the CloudSat satellite (Stephens et al., 2002), also display major differences among
78 themselves, as discussed in Li et al. (2008) and Waliser et al. (2009). While models and satellite retrievals agree that
79 the LWP and IWP should be defined as the vertically-integrated liquid and ice water content, including all
80 nonprecipitating and precipitating hydrometeors, this is not always the case in practice, further challenging a clearly-
81 posed data-data and model-data comparison. Defining the LWP and IWP varies between models, depending on the
82 complexity of the parameterization of cloud microphysics processes and prognostic versus diagnostic treatment of
83 falling hydrometeors. Defining the measured LWP and IWP varies between satellite products, depending on the
84 sensitivity of the observing systems to detect large precipitating particles. While comparing simulated and observed
85 LWP and IWP may not be as straightforward as comparing the top-of-the-atmosphere (TOA) radiation budget (Dolinar
86 et al., 2015; Stanfield et al., 2015), it offers a different way to directly diagnose biases in simulated total cloud liquid

87 and ice water mass as a first step to help correct deficiencies in parameterizing global scale moist processes and
88 precipitation.

89 Before the launch of the CloudSat and Cloud-Aerosol Lidar and Infrared Pathfinder Satellite Observation mission
90 (Stephens et al., 2002), global estimates of the LWP and IWP were retrieved principally from satellite radiance
91 measurements over different spectral intervals (e.g., Alishouse et al., 1990; Greenwald et al., 1993; Minnis et al., 1995;
92 Platnick et al., 2003). In their critical review of most common methods developed to retrieve cloud and precipitation
93 properties from satellite radiances, Stephens and Kummerow (2007) identify two main sources of errors. The first
94 source of errors originates from the mandatory classification between cloudy and cloud-free scenes, and between
95 precipitating and non-precipitating cloudy scenes. The second source of errors stems from using forward radiative
96 transfer models that lack details of the vertical distribution of cloudiness and precipitation as well as complexity in
97 specifying the optical properties of liquid water and ice particles. Estimating the LWP and IWP from CloudSat radar
98 reflectivity alone presents its own set of challenges for scenes that include precipitating cloud systems due to the high
99 sensitivity of radar reflectivity to the presence of large particles, for scenes that include mixed-phase and deep
100 convective clouds, and close to the surface due to ground clutter. Li et al. (2018) show that annual mean maps of
101 MODIS- and CloudSat-based LWP agree relatively well in tropical and subtropical regions if both data sets exclude
102 LWP observations for deep convective/precipitating clouds since MODIS is quite insensitive to precipitation.
103 Stephens and Kummerow (2007) advocate combining satellite-retrieved radar and radiance measurements to help
104 validate simulated cloud properties and precipitation. In addition to considering the impact of precipitating particles,
105 Waliser et al. (2009) demonstrate that a well-posed model-data comparison must include a consistent sampling
106 between model outputs and satellite data to reduce diurnal sampling biases and sensitivity of the sensor and retrieval
107 algorithm to the particle size when computing the simulated LWP and IWP.

108 Contemporary climate and NWP GCMs (Giorgetta et al., 2018; Molod et al., 2012; Kay et al., 2015, Skamarock
109 et al., 2012) categorize moist processes into three distinct parameterizations, one to simulate turbulent mixing in the
110 Planetary Boundary Layer (PBL) in response to surface forcing and forcing in the free troposphere, one to simulate
111 subgrid scale shallow and deep convection, and one to include grid-scale cloud microphysics. While coupling between
112 parameterizations varies between GCMs, it is an established practice to let detrained condensates from convective
113 updrafts serve as sources for non-convective grid-scale clouds, as precipitating anvils and cirrus outflow. We suggest
114 that uncertainties in parameterizing moist convection and impact on grid-scale clouds may explain a major part of the
115 differences in the LWP and IWP simulated between the CMIP3 and CMIP5 GCMs. In recent years, efforts have been
116 made to develop unified cloud parameterizations to represent all cloud types and alleviate the need to parameterize
117 complex interactions between stratiform, shallow convective, and deep convective clouds (Guo et al., 2015; Storer et
118 al., 2015; Thayer et al., 2015). Using the global Model for Prediction Across Scales (MPAS; Skamarock et al., 2012),
119 Fowler et al. (2016) discuss the sensitivity of simulated precipitation as spatial resolution increases from hydrostatic
120 to nonhydrostatic scales and suggest to further analyze the associated sensitivity of simulated clouds and TOA
121 radiation. Results show that as subgrid scale convective motions are increasingly resolved, diagnostic precipitation
122 from the scale-aware Grell-Freitas (GF; Grell and Freitas, 2014) deep convection scheme decreases while prognostic
123 precipitation from the WSM6 (Hong and Lim, 2006) cloud microphysics scheme increases over the refined area of

124 the variable-resolution mesh. Vertical profiles of the cloud liquid and ice water mixing ratios and cloud fraction
125 highlight the redistribution of cloud condensates and relative humidity with height in the refined area in response to
126 decreased contribution of convective detrainment of cloud liquid water and ice. However, Fowler et al. (2016) do not
127 further address if variations in the vertical profiles of cloud condensates lead to improved LWP, IWP, and cloud optical
128 properties against satellite-derived data.

129 The objectives of our research are threefold. First, we want to assert that our suite of PBL, deep and shallow
130 convection, and cloud microphysics parameterizations tested in MPAS at hydrostatic and nonhydrostatic scales for
131 medium-range spring forecasts over the Continental United States (Schwartz, 2019; Wong and Skamarock, 2016) can
132 also be used to produce month-long simulations of tropical convection, narrowing our analysis on the Tropical Pacific
133 Ocean. In order to broaden our research and possibly generalize our results, we also implemented the scale-aware
134 MultiScale Kain-Fritsch (MSKF; Glotfelty et al., 2019; Zheng et al., 2016) parameterization of deep and shallow
135 convection in addition to GF. Second, we want to evaluate the ability of MPAS to simulate the LWP, IWP, cloudiness,
136 and TOA long- and short-wave radiation against the Clouds and the Earth’s Radiant Energy System (CERES; Wielicki
137 et al., 1996) Single Scanner FootPrint (SSF; Minnis et al., 2011) data set, and precipitation against the TRMM
138 Multisatellite Precipitation Analysis (TMPA; Huffman et al., 2007). Our third goal aims at understanding differences
139 in the LWP, IWP, precipitation, and cloud radiative effects as functions of horizontal resolution with GF and MSKF
140 using the capability of local mesh refinement developed for MPAS.

141 In Section 2, we summarize the characteristics of the GF and MSKF parameterizations of deep and shallow
142 convection. In Section 3, we provide a short description of MPAS, including physics parameterizations used with both
143 convective parameterizations, the design of our experiments using the uniform- and variable-resolution meshes, and
144 description of the satellite data sets used to validate our results. In Section 4, we analyze our results in terms of
145 precipitation and varying contribution of the convective and grid-scale precipitation to the total precipitation as a
146 function of horizontal resolution. In Section 5, we compare the LWP, IWP, and TOA long- and short-wave radiation
147 against satellite data. In Section 6, we discuss some of our findings. Finally, in Section 7, we summarize our results
148 and propose areas of future research.

149 **2 Description of the convective parameterizations**

150 Mass flux-based convective parameterizations distinguish themselves through the use of different triggering
151 functions to initiate convection, the details of their entraining-detraining cloud models, and formulation of their
152 closures that control the intensity of convection and computation of the cloud base mass flux. For convective
153 parameterizations that include deep and shallow convection, criteria that characterize the two kinds of convection
154 strongly vary. Furthermore, how convective parameterizations account for the dependence of convection on the
155 horizontal resolution differs in complexity. In this section, we summarize the chief characteristics of GF and MSKF,
156 including differences in their treatment of deep and shallow convection, and horizontal-scale dependence.

157 2.1 The Grell-Freitas (GF) parameterization

158 The version of GF used in our numerical experiments is that implemented in version 3.8.1 of the Advanced
159 Research Weather Research Forecast model (Skamarock et al., 2008), as described in Grell and Freitas (2014). Its
160 properties are first discussed in Grell (1993) and later expanded in Grell and Devenyi (2002) to include stochasticism.
161 GF treats deep and shallow convection separately by using different initial entrainment rates ($7 \times 10^{-5} \text{ m}^{-1}$ and 1×10^{-2}
162 m^{-1} for deep and shallow convection, respectively) to control the depth of convective layers and different closures to
163 calculate the cloud base mass flux. GF includes an ensemble of closures from well-known convective
164 parameterizations to compute a mean cloud-base mass flux. For deep convection, these four closures are the *AS* closure
165 (Arakawa and Schubert, 1974) that assumes instantaneous equilibrium between the large-scale forcing and subgrid-
166 scale convection; the *W* closure (Brown, 1979; Frank and Cohen, 1987) that relates the cloud base mass flux to the
167 grid-scale upward vertical velocity; the *MC* closure (Krishnamurti et al., 1983) that calculates the cloud base mass
168 flux as a function of the vertically-integrated vertical moisture advection; and the *KF* closure (Kain and Fritsch, 1993)
169 that reduces the convective available potential energy over a prescribed convective time-scale. Qiao and Liang (2015)
170 analyze the separate and combined impacts of the four closures on the simulated summer precipitation over the United
171 States coastal oceans. On the one hand, they found that computing the cloud base mass flux using the *W* and *MC*
172 closures led to precipitation patterns and amounts that are in better agreement against TMPA data than those using the
173 *AS* and *KF* closures. On the other hand, they found that the *AS* and *KF* closures yield improved diurnal cycle of
174 precipitation relative to the other two closures. In our numerical experiments, GF gives an equal weight to each closure
175 to calculate the mean cloud base mass flux for deep convection. As for deep convection, GF includes different closures
176 for shallow convection. In our numerical experiments using GF, we choose the boundary layer quasi-equilibrium
177 (*BLQE*) closure of Raymond (1995) for shallow convection.

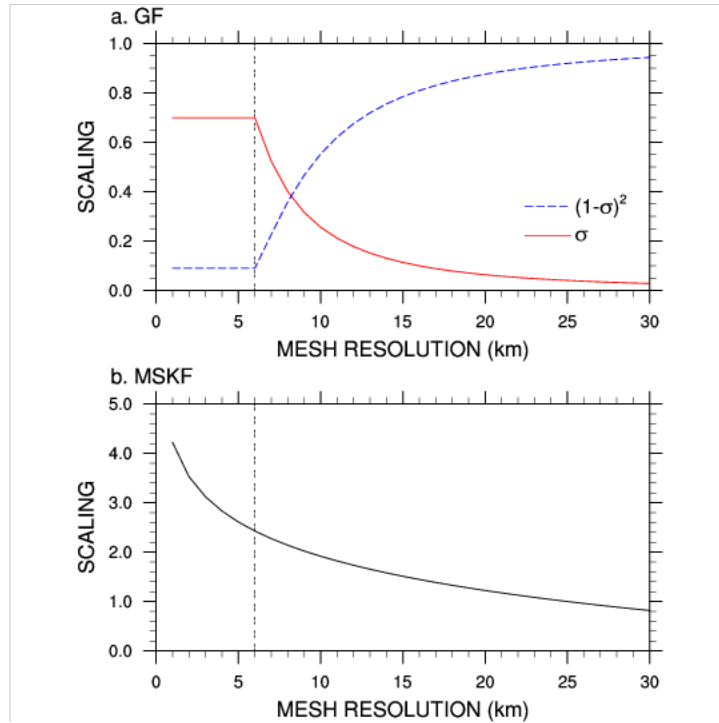
178 Both types of convection transport total water and moist static energy in a conservative manner but neglect to
179 include ice phase processes in updrafts and downdrafts. In this version of GF, the only feedback between shallow
180 convection and the large-scale environment is lateral and cloud-top detrainment of water vapor and corresponding
181 heating, as liquid water formed in shallow updrafts evaporates immediately. Deep convection returns potential
182 temperature, water vapor, and condensed water tendencies to the environment. Detrained condensed water acts as a
183 source of liquid water (ice) if the large-scale temperature is warmer (colder) than the prescribed 258 K threshold.
184 While GF assumes that shallow convective plumes are not deep enough to produce precipitation, the conversion of
185 liquid water to rain water in deep convective plumes depends on a simple Kessler-type (Kessler, 1969) conversion
186 threshold and precipitation reaches the surface instantaneously.

187 As discussed in Grell and Freitas (2014), deep convection includes a simplified representation of the unified
188 parameterization of deep convection described in Arakawa and Wu (2013). Arakawa and Wu (2013) demonstrate that
189 mass flux-based convective parameterizations can be modified to work at all resolutions spanning between hydrostatic
190 and nonhydrostatic scales through the reduction of the convective vertical eddy transport as a quadratic function of
191 the horizontal fraction of the grid box occupied by convective updrafts. In GF, the convective updraft fraction (σ) is

192 computed as a simple function of the initial entrainment rate ($\varepsilon = 7 \times 10^{-5} \text{ m}^{-1}$) and half-width radius (R) of convective
 193 updrafts following Simpson and Wiggert (1969), or

$$194 \quad \sigma = \frac{\pi R^2}{A} \quad \text{and} \quad R = \frac{0.2}{\varepsilon} \quad (1)$$

195 where A is the area of the grid box. In Eq. (1), σ is not allowed to exceed 0.7, based on the discussion of Grell and
 196 Freitas (2014). As discussed in Fowler et al. (2016), when σ becomes greater than 0.7, σ is set to 0.7 and ε is
 197 recalculated using Eq. (1), leading to increased entrainment and decreased convective cloud-tops as A becomes
 198 smaller. Another option would be to turn off deep convection when σ reaches values close to 1, in which case a better
 199 choice for its maximum value may be between 0.9 and 1 (Grell and Freitas, 2014). Figure 1.a highlights the rapid
 200 decrease in σ from 0.7 to 0.3 as spatial resolution decreases from 6 to 9 km. σ further decreases from 0.3 to 0.1 for
 201 resolutions between 9 and 16 km, and from 0.1 to 0.05 for resolutions between 16 and 30 km. The $(1-\sigma)^2$ quadratic
 202 function used to scale the mass flux starts to be significant at resolutions greater than 20 km and decreases rapidly to
 203 a minimum value of 0.1 for horizontal grid-spacing smaller than 6 km. Using a maximum value for σ ensures that
 204 over the most refined area of the mesh, parameterized deep convection is not completely turned off since deep
 205 convection is not explicitly resolved. Using a variable-resolution mesh varying between 50 km over the coarse area
 206 of the mesh down to 3 km over the refined area of the mesh centered over South America, Fowler et al. (2016) show
 207 that the impact of parameterized deep convection weakens and that of grid-scale cloud microphysics strengthens as
 208 horizontal grid-spacing increases from hydrostatic to nonhydrostatic scales.



209 **Figure 1:** a) Convective updraft fraction as a function of the mesh resolution used to scale the cloud base mass flux in GF; and b)
 210 scaling factor as a function of the mesh resolution used to scale the convective time-scale in MSKF.
 211

212 2.2 The Multi-Scale Kain-Fritsch (MSKF) parameterization

213 MSKF is the scale-aware version of the Kain-Fritsch (KF) convective parameterization, first developed by Kain
214 and Fritsch (1990; 1993), and later updated by Kain (2004) to include, among other improvements, non-precipitating
215 shallow convection. The trigger function is that used in Fritsch and Chappell (1980), originally tested in Kain and
216 Fritsch (1992) and recently in Suhas and Zhang (2014). In MSKF, convection may be triggered if the temperature of
217 a *mixed layer* is greater than that of the environment. The pressure thickness of that mixed layer must be at least 50
218 hPa thick and is computed as the sum of adjacent layer depths starting at the layer next to the surface. The mixed layer
219 temperature is a pressure-weighted function of the temperatures in those adjacent layers after being lifted to the Lifting
220 Condensation Level (LCL) plus a perturbation temperature linked to the magnitude of the grid-scale vertical motion
221 at the LCL. Once the base of a potential updraft source layer is found, convection remains activated if the vertical
222 velocity of an air parcel lifted using the Lagrangian parcel method remains positive for a minimum cloud depth of 3
223 km, as a test that the convective instability is strong enough for the air parcel to reach the Level of Free Convection
224 (LFC). If not, the procedure is repeated by moving up to the next model layer until a new updraft source layer is found
225 or until the search reaches above the lowest 300 hPa of the atmosphere. Further details on the equations used to
226 compute the perturbation temperature and parcel vertical velocity are found in Kain (2004).

227 In MSKF, the closure assumption assumes that the Convective Available Potential Energy in a cloud layer is
228 removed within a time adjustment period following Bechtold et al. (2001). The convective time-scale is defined as the
229 advective time-scale in the cloud layer with maximum values of 1 h and 0.5 h for deep and shallow convection,
230 respectively. In contrast to GF, the thermodynamics inside the cloud model includes the ice phase. The condensed
231 water formed in each cloudy layer is partitioned between liquid water and ice, assuming a linear transition of the cloud
232 temperature between 268 K and 248 K. A fraction of the condensed water converts to rain, following Ogura and Cho
233 (1973), and reaches the ground instantaneously. As discussed in Kain (2004), when an updraft source layer is
234 identified, the classification of a convective cloud layer as deep or shallow depends on the cloud depth. Shallow
235 convection is activated when all the criteria for deep convection are met, but the depth of the updraft is shallower than
236 the minimum cloud depth (3 km). This definition implies that shallow and deep convection are not allowed to coexist.
237 In the case of shallow convection, precipitation formed in updrafts is detrained to the environment as rain or snow,
238 providing an additional moisture source to the large-scale environment. As in GF, MSKF provides tendencies of
239 temperature, water vapor, cloud liquid water/ice to the environment, and tendencies of rain and snow from shallow
240 convection.

241 MSKF contains many improvements over KF, as summarized in the supplemental material of Glotfelty et al.
242 (2019). These improvements include subgrid-scale cloud feedbacks to radiation from both shallow and deep
243 convection leading to more realistic surface downward radiation, as described in Alapaty et al. (2012), and the scale
244 dependence of fundamental parameters so that MSKF can be used at spatial resolutions varying between hydrostatic
245 and nonhydrostatic scales. As detailed in Glotfelty et al. (2019) and Zheng et al. (2016), MSKF uses a scale dependent
246 formulation (β) to the adjustment time-scale (τ) for deep and shallow convection based on Bechtold et al. (2008), or

$$247 \quad \tau = \frac{H}{w_{cl}} \beta \quad \text{and} \quad \beta = 1 + \ln\left(\frac{25}{\Delta x}\right) \quad (2)$$

248 where H and W_{cl} are the depth of the convective cloud and cloud-averaged vertical velocity scale, and Δx is the grid
249 spacing. Figure 1.b highlights the dependence of the β scaling parameter as a function of horizontal resolution. As
250 many MSKF parameters are optimized for a resolution around 25 km (Kain, 2004), β is equal to 1 at 25 km, ramping
251 up to values greater than 2.4 for resolutions higher than 6km. Because the adjustment time-scale is proportional to
252 β (Zheng et al., 2016), it increases as horizontal resolution increases, leading to scale-aware stabilization of the
253 atmosphere by MSKF. In addition, MSKF includes a new scale-aware formulation of the minimum entrainment rate
254 using the LCL as a function of the scale-dependent *Tokioka* parameter (Tokioka et al., 1988), a scale-dependent
255 conversion rate for liquid water and ice condensates to precipitation, an increased grid-scale velocity expressed in
256 terms of the subgrid scale updraft mass flux, and elimination of double counting of precipitation in cloudy layers. The
257 separate and combined impacts of the development of MSKF on high resolution weather forecasts and regional climate
258 simulations are discussed in Herwehe et al. (2014), Mahoney (2016), He and Alapaty (2018), Zheng et al. (2016), and
259 Glotfelty et al. (2019).

260 **3 Methodology**

261 **3.1 Numerical experiments**

262 We discuss differences in our MPAS results between GF and MSKF configurations on precipitation, cloud
263 properties, and TOA radiation using 30-day long numerical experiments in MPAS (Skamarock et al., 2012). MPAS
264 is a global nonhydrostatic atmospheric model developed for NWP and climate studies. The horizontal discretization
265 uses an unstructured spherical centroidal Voronoi tessellation with a C-grid staggering, as described in Ju et al. (2011),
266 while the vertical discretization is the height-based hybrid terrain-following coordinate of Klemp (2011). The
267 dynamical solver integrates the prognostic equations (cast in flux form) for the horizontal momentum, vertical
268 velocity, potential temperature, dry air density, and scalars using the split-explicit technique of Klemp et al. (2007).
269 The temporal discretization uses a third-order Runge-Kutta scheme and the explicit time-splitting technique described
270 in Wicker and Skamarock (2002). We use the monotonic option of the scalar transport scheme of Skamarock and
271 Gassmann (2011) for horizontal and vertical advection of all moist scalars on the unstructured Voronoi mesh. Finally,
272 horizontal filtering of the state variables is based on Smagorinsky (1963), as described in Skamarock et al. (2012). For
273 variable-resolution meshes, the eddy viscosity coefficient is scaled as a function of the inverse mesh density so that
274 horizontal diffusion is increased in the coarse area relative to the refined area of the mesh.

275 In MPAS, the computational flow includes three distinct steps. The first step calls the physics parameterizations
276 that update the surface energy budget and calculate the tendencies of potential temperature, moist species, and zonal
277 and meridional wind due to long- and short-wave radiation, sub-grid scale convection, condensation and mixing in
278 the PBL and free troposphere, and gravity wave drag due to orography. The physics parameterizations use the same
279 input surface boundary conditions and soundings to compute their respective tendencies. Besides GF and MSKF, these
280 parameterizations are,

- 281 • the Noah land surface parameterization described by Chen and Dudhia (2001),

- 282 • the long- and short-wave Rapid Radiative Transfer Model for GCMs (RRTMG) described by Mlawer et al. (1997)
- 283 and Iacono et al. (2000),
- 284 • the semi-empirical parameterization of the cloud fraction of grid-scale clouds from Xu and Randall (1996) and
- 285 convective clouds from Xu and Krueger (1991) for use in the long- and short-wave RRTMG schemes. Following
- 286 Xu and Randall (1996), the fractional amount of grid-scale clouds is a function of the relative humidity and grid-
- 287 averaged condensate mixing ratio of cloud liquid water, ice, and snow. In MSKF, the fractional amount of shallow
- 288 and deep convective clouds depends on the convective mass flux.
- 289 • the Mellor–Yamada–Nakanishi–Niino (MYNN) Planetary Boundary Layer (PBL) and surface layer scheme
- 290 described by Nakanishi and Niino (2009) with many updates described in Olson et al. (2019), and
- 291 • the gravity wave-drag parameterization of Hong et al. (2008).

292 The second step calls the dynamical solver which updates the state variables with their respective diabatic

293 tendencies in conjunction to applying horizontal and vertical advection. Finally, the third step calls the grid-scale cloud

294 microphysics parameterization so that at the end of the model time-step, supersaturation has been entirely removed or

295 the relative humidity does not exceed 100%. Unlike the physics parameterizations listed in step one, the grid-scale

296 cloud microphysics scheme updates the potential temperature and moist species for the next time-step instead of

297 providing individual tendencies. The bulk cloud microphysics parameterization of Thompson et al. (THOM; 2004,

298 2008) is used in all our numerical experiments. THOM includes prognostic equations for temperature, mass mixing

299 ratio of water vapor, cloud liquid water, rain, cloud ice, snow, and graupel, and number concentration of cloud ice and

300 rain. We set the number concentration of cloud droplets to $300 \times 10^6 \text{ m}^{-3}$ over land and $100 \times 10^6 \text{ m}^{-3}$ over oceans. In

301 RRTMG, we diagnose the radiative effective radii of cloud liquid water, cloud ice, and snow as functions of the

302 THOM cloud particle assumptions to add coupling between the cloud microphysics and cloud optical properties, as

303 discussed in Thompson et al. (2016).

304 To compare the two convective parameterizations against satellite-derived data at hydrostatic scales, we use a

305 quasi-uniform resolution mesh for which the mean distance between cell centers is 30 km, corresponding to 655,362

306 cells. The vertical scale includes 55 layers with monotonically increasing thicknesses varying from 50 meters next to

307 the surface to 700 meters below 10 km to 1000 meters below the model top over ocean cells. The model top is set at

308 30 km. The dynamics and physics time-steps are both set to 150 s, and the horizontal diffusion length scale is set to

309 30 km. Long- and short-wave radiation is called every 15 mins and THOM is cycled twice so that the cloud

310 microphysics time-step is less than 90 s to ensure computational stability (Thompson, private communication). With

311 each convection scheme, we have performed a one-month long experiment preceded by a two-day spin-up to simulate

312 Northern Hemisphere early winter, initializing our experiments with ERA-Interim (Dee et al., 2011) reanalyses for

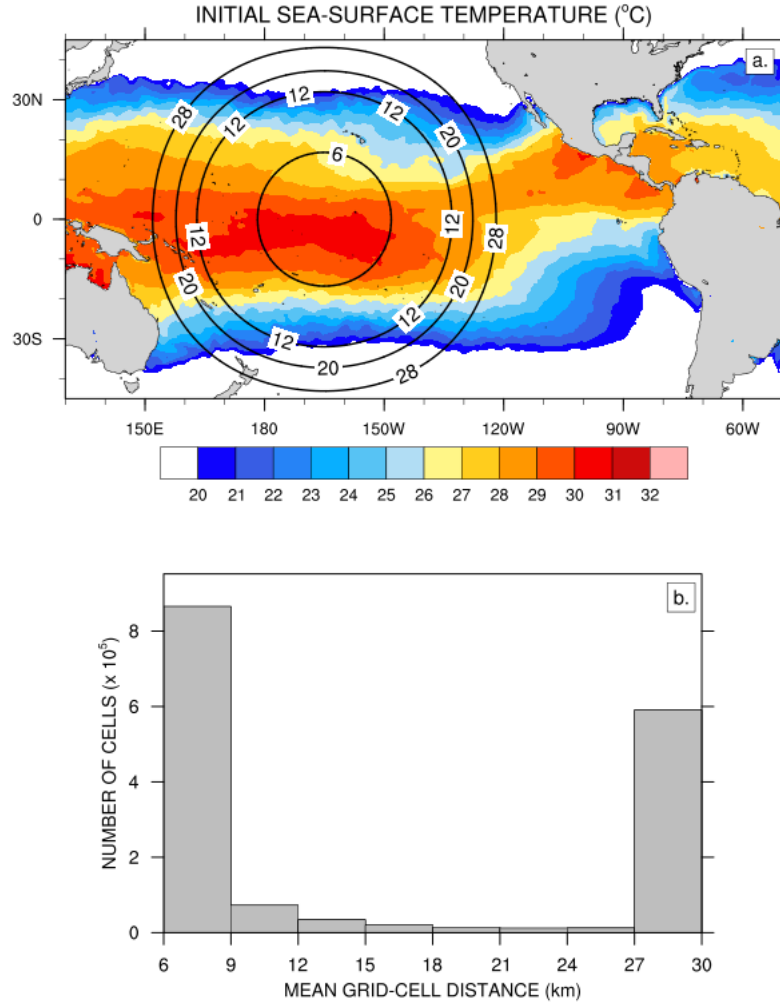
313 0000 UTC 29 November 2015. ERA-Interim sea surface temperatures and sea ice fractions are used to update ocean

314 cells daily. We refer to our quasi-uniform resolution experiments run with GF and MSKF as GFu and MSKFu,

315 respectively.

316 **3.2 Sensitivity experiments**

317 Using a variable-resolution mesh spanning between 50 km and 3 km in MPAS, Fowler et al. (2016) demonstrate
318 that subgrid-scale convection parameterized with GF weakens and grid-scale cloud microphysics parameterized with
319 WSM6 (Hong and Lim, 2006) strengthens as resolution increases from the coarse to the most refined area of the mesh.
320 Over the most refined area, grid-scale precipitation contributes a major part to total precipitation, and vertical profiles
321 of subgrid-scale deep convective heating and drying resemble those obtained with a precipitating shallow convection
322 scheme. Fowler et al. (2016) suggest investigating the effect of variable resolution on cloud macrophysical properties
323 and TOA radiation, as grid-scale cloud microphysics parameterizations provide a more physically-based description
324 of condensation and precipitation over the refined area of the mesh, compared to simpler entraining-detraining cloud
325 models used in parameterized convection schemes. With the aim to quantify changes in cloud properties and radiation
326 across scales using GF and MSKF, we repeat the early winter experiments but with a variable-resolution mesh that
327 spans between 30 km and 6 km and includes 1,622,018 cells. As shown in Fig. 2.a, we center the refined area of the
328 mesh over the Pacific warm pool defined as the area of the Western Pacific Ocean where sea-surface temperatures
329 (SSTs) exceed 28.5°C, or between 170°E and 140°W. East of 140°W, the north-south width of warmest SSTs across
330 the transition zone between the refined and coarse mesh narrows to delineate the location of the ITCZ in the Tropical
331 Eastern Pacific. West of 170°E, the end of mesh refinement borders the eastern tip of Papua New Guinea. Along the
332 Equator, the transition zone between nonhydrostatic and hydrostatic scales spans 20° in the meridional direction on
333 either side of the most refined area of the mesh.



334 **Figure 2:** a) Initial sea-surface temperature and refined variable-resolution mesh depicted using isolines of the mean distance
 335 between grid-cell centers (km) over the Tropical Pacific Ocean; and b) histogram of the number of cells as a function of the mean
 336 distance between grid-cell centers.
 337

338 Figure 2.b displays a histogram of the mean distance between grid-cell centers. Differences between the initialization
 339 of the variable- and quasi uniform-resolution experiments include a reduced time-step from 150 s to 30 s and a reduced
 340 minimum horizontal diffusion length scale from 30 km to 6 km. Also, THOM is called only once per physics time-
 341 step. We refer to our variable-resolution experiments run with GF and MSKF as GFv and MSKFv, respectively.
 342 Differences between GFu, GFv, MSKFu, and MSKFv are listed in Table 1. We acknowledge that running single 30-
 343 day long experiments is a non-traditional way to assess the performance of convective parameterizations in an NWP
 344 framework but is needed to provide increased satellite sampling when comparing simulated clouds and precipitation
 345 against observations. Judt (2020) computes the predictability of the atmosphere using global convection-permitting
 346 simulations with the same version of MPAS as in this study, but with a global uniform mesh with a 4 km cell spacing.
 347 Results show that the predictability of the tropics (> 20 days) is longer than that of the extratropics and polar regions
 348 (~ 2 weeks) when deep convection is mostly resolved. Using the Center for Ocean-Land-Atmosphere Studies GCM
 349 with a triangular T63 truncation and the relaxed Arakawa-Schubert parameterization of deep convection (Moorthi and
 350 Suarez, 1992), Strauss and Paolino (2008) demonstrate greater predictability in the tropics than in the extratropics at

351 hydrostatic scales. As our comparison between experiments and satellite data focuses on the tropical Pacific Ocean,
 352 we are confident that biases arising during the first 2 weeks persist at longer time-scales and remain clearly depicted
 353 in their monthly means. In order to further assess the robustness of our results, we also compare the 30-day versus 10-
 354 day mean LWP, IWP, and precipitation to ensure that biases discussed in Sections 4 and 5 are qualitatively similar as
 355 those observed at shorter time-scales (not shown for brevity).

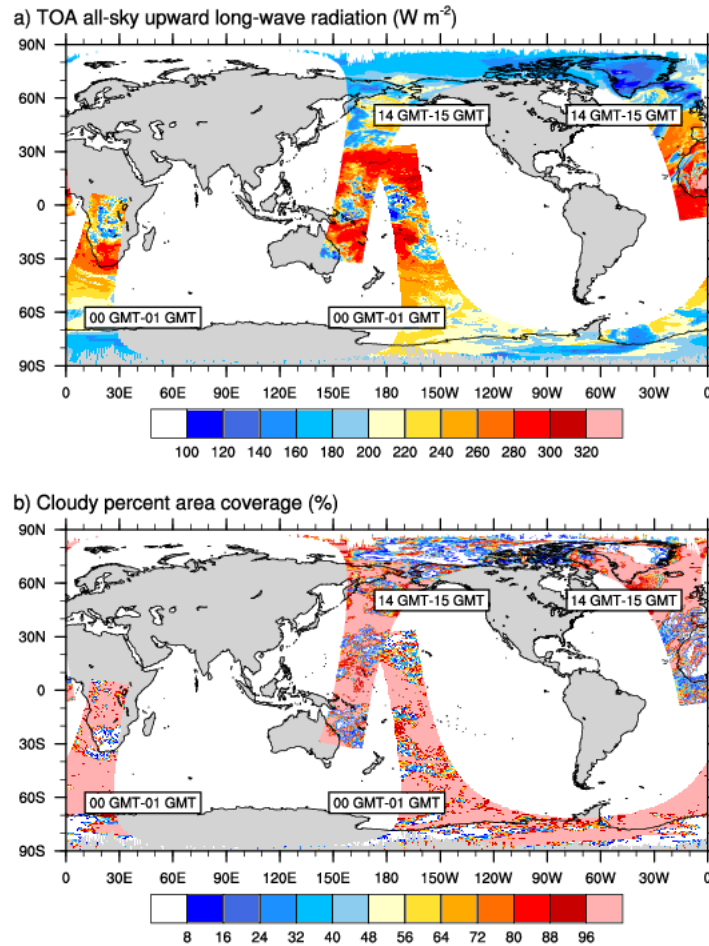
	GFu	MSKFu	GFv	MSKFv
No. of cells	655,362	655,362	1,622,018	1,622,018
Min. cell distance (km)	22.8	22.8	4.4	4.4
Max. cell distance (km)	31.8	31.8	37.8	37.8
Time-step (s)	150	150	30	30
Minimum diffusion length scale (km)	30	30	6	6
CP	GF	MSKF	GF	MSKF

356 **Table 1:** Horizontal mesh resolution, minimum and maximum distance between grid-cell centers, time-step, horizontal diffusion
 357 length scale, and convective parameterization (CP) for numerical experiments with the quasi uniform- and variable-resolution
 358 meshes.

359 3.3 Satellite data sets

360 We compare the cloud liquid water path (LWP) and ice water path (IWP), cloud area fraction (CF), and the top-
 361 of-the-atmosphere longwave upward (TOALW) and shortwave net (TOASW) radiation simulated in our numerical
 362 experiments against the Edition-4 Single Scanner Footprint (SSF) products from the Clouds and the Earth’s Radiant
 363 Energy System (CERES; Wielicki et al., 1996). Minnis et al. (2011) describe in great details the retrieval of
 364 simultaneous and collocated radiation fluxes and cloud properties from the CERES radiometers and the Moderate-
 365 resolution Imaging Spectroradiometer (MODIS) using consistent algorithms and calibration across satellite platforms,
 366 and shared auxiliary input (temperature and humidity profiles). SSF data are available in two different formats. The
 367 first data file format contains one hour of radiation fluxes and cloud properties at the instantaneous CERES 20 km
 368 footprint level from the sun-synchronous afternoon (morning) equatorial crossing time Aqua (Terra) satellites. As
 369 illustrated in Minnis et al. (2011; their Fig. 15), the CF in each SSF is given in terms of a clear fraction, a fraction for
 370 an upper and lower cloud layer separately, and a fraction for an upper layer over a lower layer, although the overlap
 371 CF is not available and set to zero in the Edition 4 release version that we are using. The LWP, IWP, and all other
 372 cloud fields are provided for the lower and upper layers, separately. Figure 3 illustrates two orbits of the Aqua satellite,
 373 one between 00 GMT and 01 GMT, and one between 14 GMT and 15 GMT, showing the TOALW (top panel) and
 374 CF (bottom panel), after gridding the hourly orbital data to a $0.2^\circ \times 0.2^\circ$ latitude-longitude grid. Gridded radiation fluxes
 375 and cloud data are means over all SSF data contained inside each rectangular grid, after applying a linear interpolation
 376 to reduce the number of missing values. Missing values, highlighted in gray in all figures, depict rectangular grids that
 377 did not contain radiation and cloud data in any of the SSF inside the $0.2^\circ \times 0.2^\circ$ grid. As seen in Fig. 3, our gridding of
 378 the orbital data removes most of the missing data along each orbit, providing a clear depiction of the relationship

379 between the TOALW and CF for cloudy and cloud-free grid cells. Areas of high (low) TOALW coincide with areas
 380 of small (large) cloudy areas, but it is also interesting to note that areas of each orbit are characterized as overcast in
 381 conjunction with areas that are not as spatially uniform in TOALW as in CF.

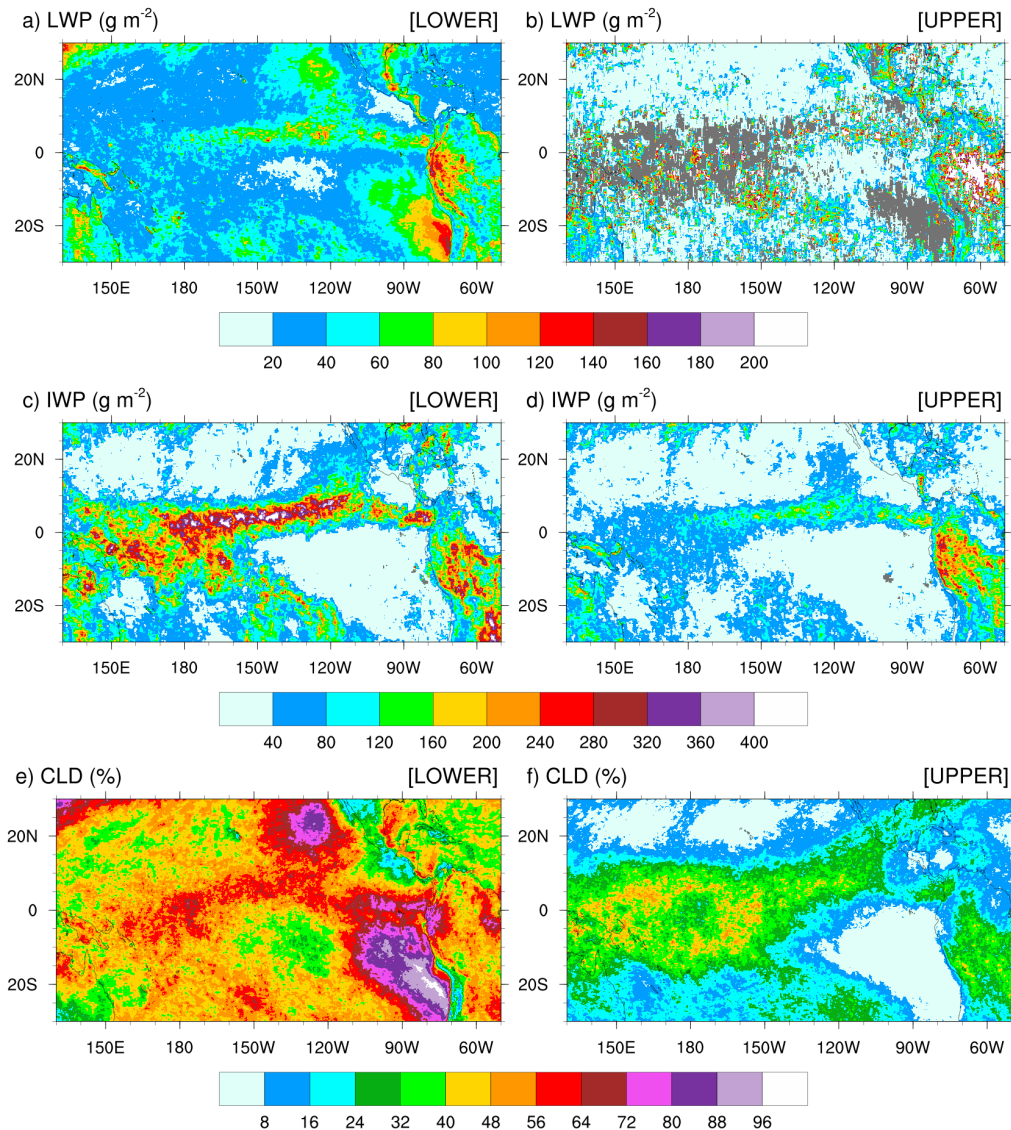


382 **Figure 3:** Orbital paths of the Aqua satellite between 00 GMT-01 GMT and 14 GMT-15 GMT after binning the SSF data onto a
 383 0.2°x0.2° rectangular grid for a) the TOA all-sky upward long-wave radiation, and b) the cloudy percent area coverage for 1st
 384 December 2015.
 385

386 The second data file format (SSF1deg) includes daily and monthly averages of the original SSF orbital data but
 387 interpolated on a 1°x1° latitude-longitude grid. The difficulty in using hourly higher-resolution orbital data instead of
 388 monthly mean lower-resolution 1°x1° latitude-longitude gridded product is that the former are available in two distinct
 389 *dynamic* layers while the latter is provided at fixed pressure levels and for the atmospheric column. The lower and
 390 upper layers are referred to as *dynamic* layers because the cloud-top (base) pressure of each layer varies between SSFs
 391 along each orbit. The advantage of using orbital hourly data is that they can be gridded and interpolated to a spatial
 392 resolution close to that of our uniform and variable-resolution numerical experiments prior to computing monthly
 393 mean radiation and cloud fields. We choose the 0.2°x0.2° latitude-longitude gridded hourly data derived from the first
 394 data file format through the entire manuscript.

395 In order to best compare the simulated against satellite-derived LWP and IWP, we need to understand the
 396 partitioning of the SSF LWP and IWP between the two cloud layers. In brief, a lower and an upper cloud layer can be

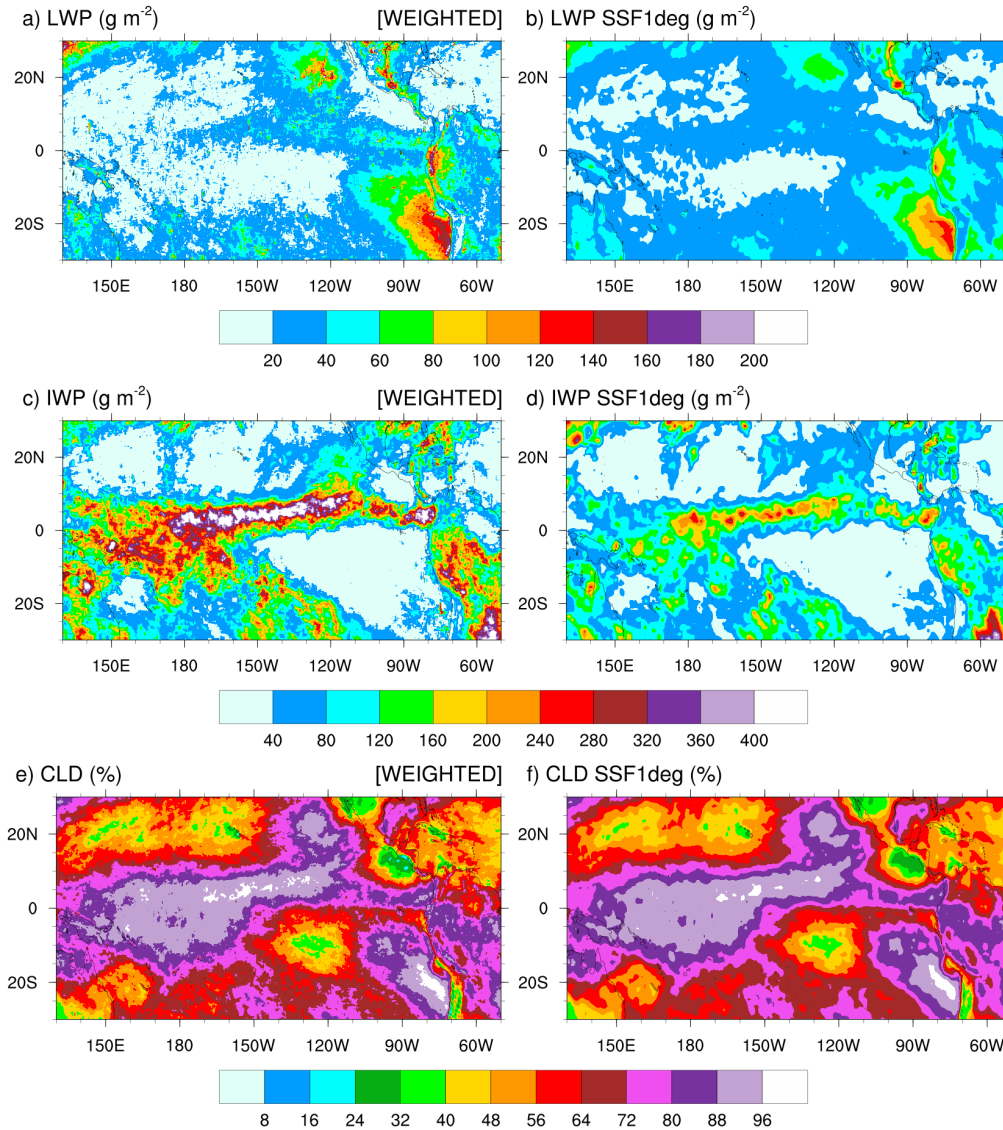
397 detected simultaneously if they lie adjacent to each other inside an SSF. In that case, the cloud properties for each
398 layer are reported separately. In the case when an opaque upper cloud layer is detected to be above a lower cloud
399 layer, it is impossible to identify the two layers separately. Then, only one cloud layer is reported and always classified
400 as the lower cloud layer, regardless of its cloud-base (top) pressure (Loeb, private communication). Further details on
401 the cloud classification, including determination of the cloud phase, are found in Geier et al. (2003) and Minnis et al.
402 (2011). Figure 4 shows the monthly-mean LWP, IWP, and CF for the lower (left panels) and upper (right panels) layer
403 measured by Aqua for December 2015 over the Tropical Pacific Ocean. Figure S1 is as Fig. 4, but for the Terra satellite
404 (see supplemental figures). LWP and IWP are *in-cloud* values meaning that they have not been weighted by CF. The
405 lower cloud layer includes stratiform clouds that form over colder sea-surface temperatures along the coast of Peru
406 and off the Baja Peninsula. Over these areas of CF greater than 72% for the lower cloudy layer, CF for the upper cloud
407 layer is less than 8%, highlighting that a single layer of low-level clouds fills a major fraction of the SSF. Increased
408 values of CF are seen in conjunction with increased (decreased) values for the LWP (IWP) in the lower cloud layer
409 indicative of warm-phase clouds, as well seen as off the coast of Peru. High values for the CF and IWP juxtaposed
410 with lower values for the LWP in the lower cloud layer depict clearly deep convection over the Eastern Pacific Ocean,
411 ITCZ, and warm pool region. Over areas of deep convection, upper cloud layers are often detected in conjunction with
412 lower cloud layers within the same SSF but are defined by decreased values for the CF and IWP. For the LWP, the
413 coexistence of a lower and upper cloud layer is quite infrequent, as seen by the number of missing grid-points in Fig.
414 4.b (S1.b). Where detected, the LWP in the upper layer exceeds that in the lower layer, indicative of warm-phase
415 mature thicker cumulus clouds coexisting with developing thinner cumulus clouds in the lower layer. Finally, outside
416 of the typical stratus cloud regions and either sides of the ITCZ and warm pool region, SSF data reveal extended
417 regions of warm-phase thinner clouds characteristic of widespread shallow convection over tropical oceans.



418
 419 **Figure 4:** Monthly-mean cloud liquid water path (LWP, top panels), cloud ice water path (IWP, middle panels), and cloud fraction
 420 (CLD, bottom panels) over the Tropical Pacific Ocean for December 2015 from the Aqua satellite. Panels a), c), and e) are for the
 421 lower cloud layer; panels b), d), and f) are for the upper cloud layer.

422 Calculating the satellite-retrieved LWP and IWP in an atmospheric column for validation of those from our
 423 numerical simulations is a two-step process. Because simulated LWPs and IWPs are *grid-cell mean* values and not
 424 *local* values, we first multiply the SSF LWP and IWP by CF to get their mean values in the lower and upper cloud
 425 layers separately, prior to gridding the hourly orbital data. Second, because the lower and upper layers are defined as
 426 adjacent to each other and never overlap in an SSF, we simply add the grid-cell mean LWP and IWP in the lower layer
 427 to that in the upper layer to compute the total LWP and IWP. Our processing method is simpler than the processing
 428 steps taken by the CERES Science Team to spatially grid and temporally average SSF hourly orbital data to SSF1deg
 429 gridded monthly mean data. Figure 5 compares the monthly-mean $0.2^\circ \times 0.2^\circ$ latitude-longitude CF-weighted LWP
 430 and IWP and CF (left panels) against the SSF1deg products (right panels) for December 2015 over the Tropical Pacific
 431 Ocean. The top panels of Fig. 5 show that our method reproduces successfully the geographical patterns and magnitude

432 of the LWP over the Tropical Pacific when compared against the SSF1deg data for both months. In contrast, because
 433 our method does not weigh the IWP as a function of height, it systematically overestimates the SSF IWP when
 434 compared against the SSF1deg data, as seen over the ITCZ and South Pacific Convergence Zone (SPCZ) in both
 435 months.
 436



437 **Figure 5:** Monthly-mean cloudy area-weighted cloud liquid water path (LWP, top panels), cloudy-area weighted cloud ice water
 438 path (IWP, middle panels), and cloud fraction (CLD, bottom panels) over the Tropical Pacific Ocean for December 2015. Panels
 439 a), c), and e) are SSF data; panels b), d), and f) are SSF1deg climatological data.
 440

441 Using ice water content data from the ascending (daytime) and descending (nighttime) portion of CloudSat orbits,
 442 Waliser et al. (2009; Fig. 7) estimate that day-night fluctuations in the ice water content at 215 hPa account for as
 443 much as 13% (20 %) of the annual mean ice water content over the warm pool (Tropical Eastern Pacific), in response
 444 to the diurnal cycle of deep convection over the tropical oceans. Therefore, when computing the monthly-mean CF,
 445 LWP, IWP, TOALW, and TOASW produced with GFu, GFv, MSKFu and MSKFv, we first sample the hourly model

446 diagnostics in accordance with the Aqua and Terra satellite orbits in order to reduce biases from different diurnal
447 sampling between our experiments and SSF data. Because the MODIS-based retrieval of the LWP and IWP is
448 insensitive to precipitation, and the rain, snow, and graupel mixing ratios are prognostic variables in THOM and fall
449 through the atmosphere at finite velocities, we infer that the LWP and IWP must include all precipitating and non-
450 precipitating condensates.

451 In addition to CERES SSF data, we use the monthly-mean precipitation rates from the TRMM Multisatellite
452 Precipitation Analysis (TMPA Version 7; Huffman et al., 2007) to compare simulated versus observed precipitation
453 rates, and monthly mean ERA-Interim reanalyses (Dee et al., 2011) to compare simulated versus observed precipitable
454 water in the lower troposphere.

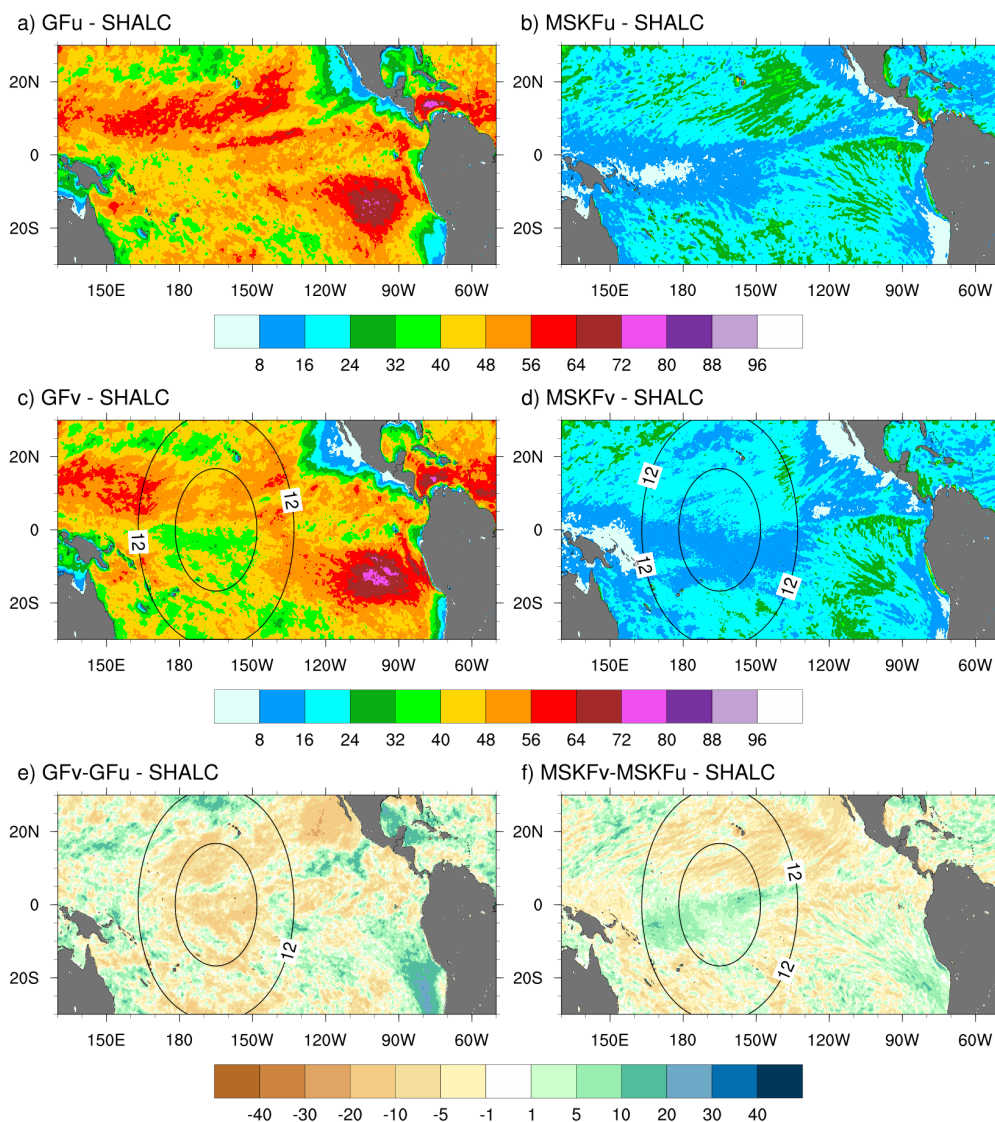
455 **4 Simulated versus satellite-retrieved precipitation**

456 **4.1 Incidence of subgrid-scale shallow and deep convection**

457 Differences in the treatment of interactions between shallow and deep convection in GF and MSKF, as described
458 in Section 2, are bound to modify the partitioning between shallow and deep convection as spatial resolution increases
459 over the refined area of the mesh. A useful diagnostic to analyze the response of shallow and deep convection to local
460 mesh refinement is the incidence of convection. Because shallow convection in both GF and MSKF is non-
461 precipitating, we set the incidence of shallow convection to 100 % when cloud-tops of shallow convective updrafts
462 are detected, and 0 % otherwise. We set the incidence of deep convection to 100 % when convective precipitation
463 occurs and 0 % otherwise. Figures 6 and 7 highlight the impact of the horizontal scale dependence of convection on
464 the monthly-mean incidence of subgrid-scale shallow and deep convection in our uniform- and variable-resolution
465 experiments for December 2015.

466 Figure 6 shows that simulated shallow convection occurs over the entire Tropical Pacific, and that its incidence
467 is about twice as large in GFu and GFv as in MSKFu and MSKFv. In GFu and GFv, incidence in excess of 48 %
468 covers most of the Tropical Pacific, including the ITCZ and warm pool where GF allows shallow and deep convection
469 to occur simultaneously. GFu and GFv exhibit highest incidence of shallow convection off the coast of Peru where
470 persistent low-level stratiform clouds are formed. In contrast, the incidence of shallow convection in MSKFu and
471 MSKFv never exceeds 32 % over the entire domain and is less than 16 % over the ITCZ and warm pool where shallow
472 and deep convection are not allowed to coexist in MSKF. The bottom panels highlight differences in the incidence of
473 shallow convection between GFv and GFu, and MSKFv and MSKFu. Despite the fact that GF does not include a
474 spatial scale dependence in its formulation of shallow convection, GFv produces reduced shallow convection relative
475 to GFu over most of the Tropical Pacific, except most notably immediately off the coast of Peru. In contrast to GFv,
476 MSKFv yields increased incidence of shallow convection over most of the warm pool region. In MSKF, the height of
477 deep convective clouds decreases as horizontal resolution increases. As the classification between deep and shallow
478 convection is a function of cloud depth, convective clouds originally defined as deep are reclassified as shallow,
479 leading to increased incidence of shallow convection in the refined area of the mesh.

INCIDENCE OF SHALLOW CONVECTION (%)



480
 481 **Figure 6:** Monthly-mean incidence of shallow convection (SHALC) over the Tropical Pacific Ocean simulated in GFu and MSKFu
 482 (top panels) and GFv and MSKFv (middle panels), and difference in the incidence of shallow convection between GFv and GFu
 483 (bottom left panel) and MSKFv and MSKFu (bottom right panel) for December 2015.

484 In Fig. 7, the top and middle panels show that, in contrast to shallow convection, the incidence of deep convection
 485 has the same order of magnitude in GFu and MSKFu, and GFv and MSKFv. The top panels reveal that the incidence
 486 of deep convection is higher in MSKFu than GFu over the ITCZ and warm pool. In MSKFu, a sharp transition between
 487 areas of high and low incidence of deep convection causes areas outside of the ITCZ and warm pool to be mostly void
 488 of deep convection, as seen between 10°N and 30°N. In GFu, the incidence of deep convection is decreased over the
 489 warm pool relative to the ITCZ west of 160°W. Outside of the ITCZ and warm pool, GFu and GFv lead to higher
 490 incidence of deep convection than MSKFu and MSKFv because, in contrast to MSKF, GF allows deep and shallow
 491 convection to coexist in the same grid-cell. Middle panels highlight decreased incidence of subgrid-scale deep
 492 convection inside the refined area of the mesh over the warm pool in both GFv and MSKFv, as we expect clouds to

493 be resolved on the higher resolution grid, in conjunction with increased incidence east and west of the refined area.
 494 The decreased incidence in the refined area is more pronounced between MSKFu and MSKFv than between GFu and
 495 GFv whereas the upscaling impact of spatial refinement outside the refined area is greater in GFv than MSKFv. The
 496 scale-aware formulation in GF does not produce the same contrast between the refined and coarse mesh in GFv and
 497 GFu as that in MSKF in MSKFv and MSKFu. Fig. 7.f reveals a reduced incidence in excess of 25 % between MSKFu
 498 and MSKFv starting at resolutions higher than 12 km flanked by increased incidence of deep convection east and west
 499 of the refined area. In contrast, Fig. 7.e displays a longitudinal band of decreased incidence of deep convection between
 500 90°W and the dateline, bordered by increased deep convection north of the equator and south of 10°S. Table 2 lists
 501 the area-averaged incidence of deep and shallow convection for an area inside the refined mesh (REFINED: 0.1°N to
 502 5.1°N; 150°W to 180°W) and an area over the Tropical Eastern Pacific (EAST: 3.1°N to 8.1°N; 90°W to 120°W), as
 503 later shown in Figure 9.a. The REFINED and EAST areas display little variation in the incidence of shallow
 504 convection between GFu (MSKFu) and GFv (MSKFv), but the incidence of shallow convection in GFu and GFv is
 505 much higher than in MSKFu and MSKFv. The incidence of subgrid-scale deep convection is higher in the EAST area
 506 compared to the REFINED area in all four experiments. Over the REFINED area, the incidence of subgrid-scale deep
 507 convection remains about the same between GFu and GFv but strongly decreases between MSKFu and MSKFv.

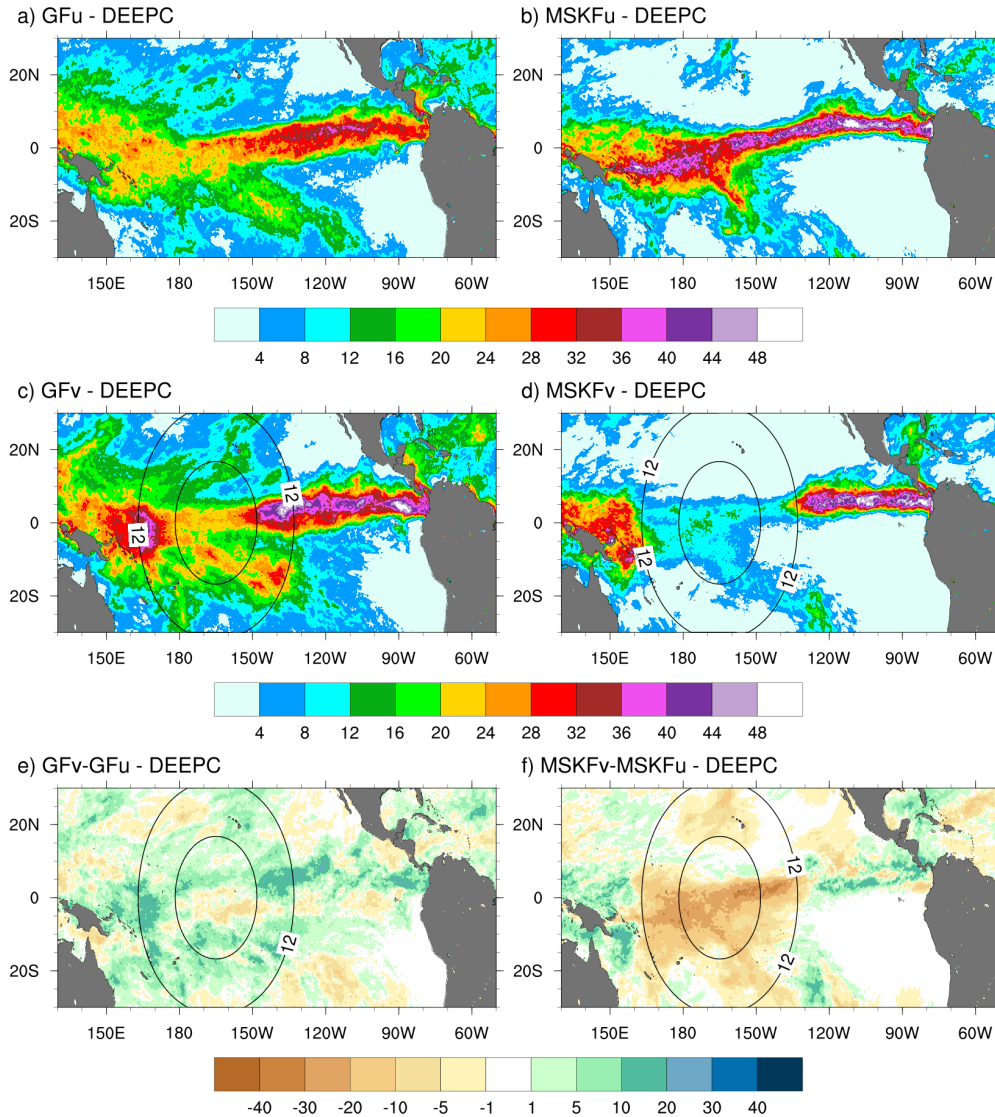
508

	DEEP CONVECTION (%)		SHALLOW CONVECTION (%)	
	REFINED	EAST	REFINED	EAST
GFu	20	30	52	52
GFv	23	36	47	48
MSKFu	27	33	14	17
MSKFv	10	36	17	15

509 **Table 2:** Area-averaged incidence of deep and shallow convection. The REFINED and EAST areas are shown in Figure 9.a.

510 As described in Section 2, MSKF differentiates shallow from deep convection as a function of the convective
 511 cloud depth. As spatial resolution increases, the scale aware formulation leads to a reduction in the intensity of
 512 convection and depth of convective clouds, mostly deep convection, over the refined area as seen in Fig. 7.f. As the
 513 depth of convective clouds originally classified as precipitating deep convective clouds become shallower, MSKF
 514 reclassifies those same clouds as nonprecipitating shallow clouds, leading to near-equal compensation between the
 515 decreased and increased incidence of deep and shallow convection over the warm pool. In contrast to MSKF, GF
 516 causes precipitating deep convection to become precipitating shallow convection at increased spatial resolution. As
 517 this process occurs in the deep convection scheme and both cloud types precipitate, variations in the incidence of deep
 518 convection between GFu and GFv are small. Further analysis of the response of shallow convection between GFu and
 519 GFv over the refined area is beyond the objectives of this research.

INCIDENCE OF DEEP CONVECTION (%)

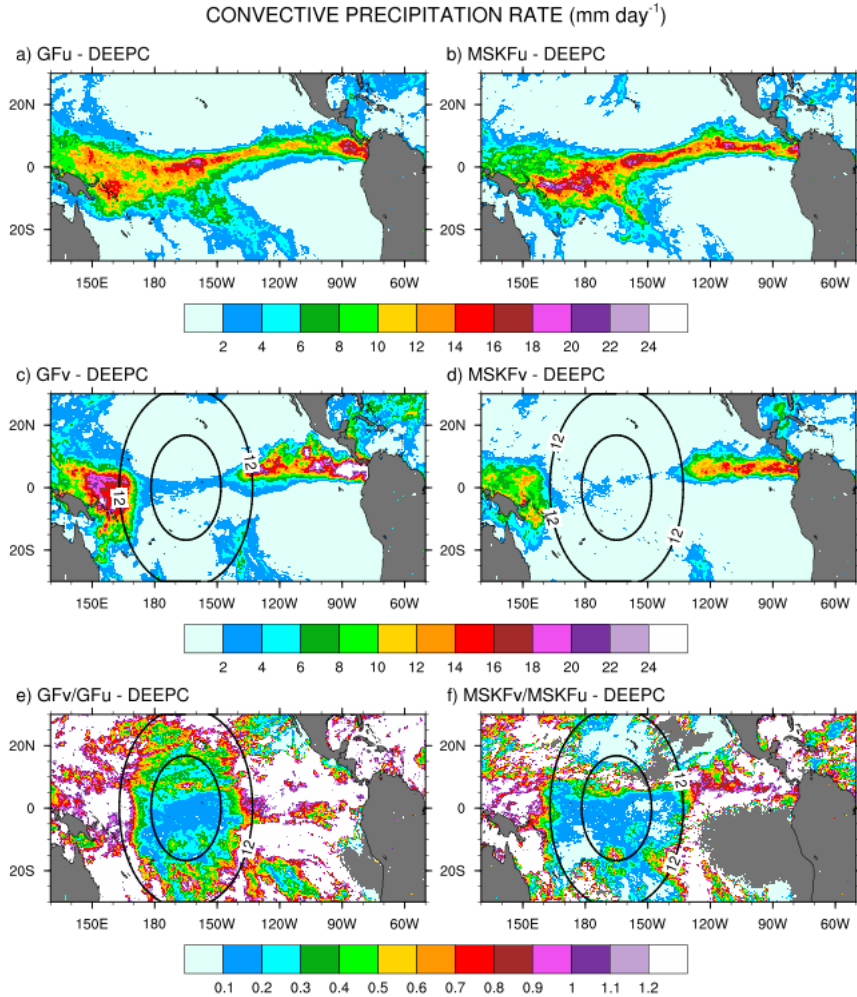


520
521 **Figure 7:** As Fig. 6, but for the monthly-mean incidence of deep convection (DEEPC).

522 **4.2 Precipitation rates**

523 Figure 8 shows the monthly-mean convective precipitation rate simulated in GFu and MSKFu (top panels), and
 524 GFv and MSKFv (middle panels). The bottom panels in Figure 8 display the ratio between the convective precipitation
 525 rate simulated in GFv (MSKFv) and GFu (MSKFu) to contrast the impact of the scale aware formulation in GF and
 526 MSKF. The top panels highlight similar geographical patterns of convective precipitation in GFu and MSKFu.
 527 Between 80°W and 160°W, increased convective precipitation is located along the ITCZ, in conjunction with
 528 increased incidence of deep convection, as seen in Figs. 7.a-b. West of 160°W, GFu leads to decreased but more
 529 widespread convective precipitation relative to MSKFu over the warm pool, in conjunction with decreased but more
 530 widespread incidence of convection. In GF, this result infers that while deep convection is not triggered as often over
 531 the warm pool as along the ITCZ, the amount of convective precipitation produced in one time-step is higher over the

532 warm pool than along the ITCZ, so that monthly-mean convective precipitation rates remain about the same in both
533 regions. In Fig. 8, and in agreement with the middle panels of Fig. 7, middle panels display a strong decrease in
534 convective precipitation in both GFv and MSKFv over the refined area of the mesh. In MSKFv, the strong reduction
535 in convective precipitation occurs, not only over the most refined area of the mesh, but also where horizontal grid-
536 spacing increases from 6 to 12 km. In GFv, convective precipitation increases sharply as soon as grid-spacing is greater
537 than 12 km and exceeds that simulated in GFu over the coarse area of the mesh. In GFv, the monthly-mean convective
538 precipitation rate is higher than that in MSKFv over the most refined area of the mesh but starts to increase more
539 rapidly between 6 and 12 km than in MSKFv. Differences in increasing convective precipitation across the transition
540 zone between the refined and coarse areas reflect different impacts of the scale-aware formulation in GF and MSKF.
541 The bottom panels in Figure 8 show that the ratio in convective precipitation between GFv and GFu has the same
542 order of magnitude as that between MSKFv and MSKFu over the refined area of the mesh. While it remains as small
543 in the transition zone as in the refined mesh with MSKF, this ratio increases to values greater than 1 between 6 and
544 12 km with GF, indicating increased convective precipitation on each side of the refined area in GFv relative to GFu,
545 as also seen in Figure 8.c. Maps of monthly-mean grid-scale precipitation rates show similar geographical patterns
546 between GFu and MSKFu. Over the refined area, increased grid-scale precipitation compensates decreased convective
547 precipitation in both GFv and MSKFv. Over the coarse area, grid-scale precipitation decreases along the ITCZ and
548 warm pool in GFv while remaining nearly the same in MSKFv (not shown for brevity).

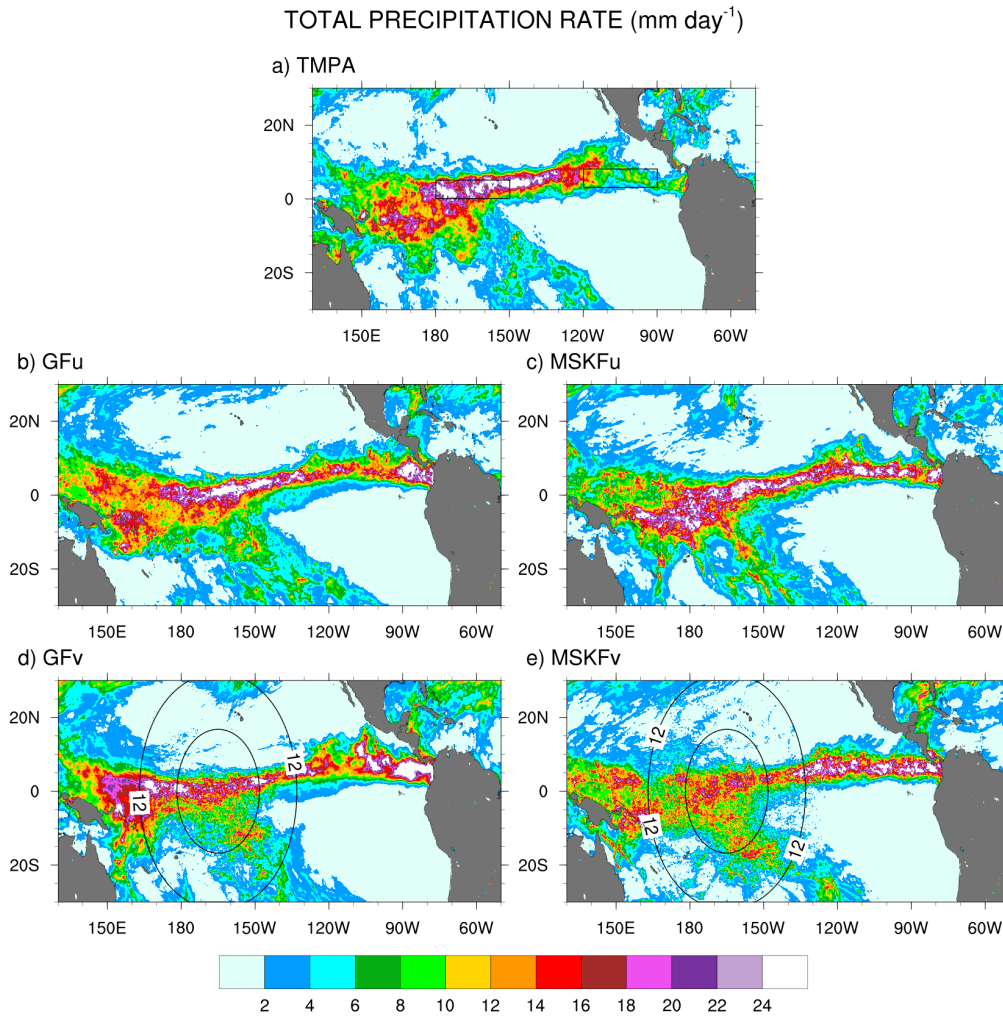


549

550 **Figure 8:** Monthly-mean convective (DEEPC) precipitation rate over the Tropical Pacific Ocean simulated in GFu and MSKFu
 551 (top panels), GFv and MSKFv (middle panels), and ratio between the monthly-mean convective precipitation rate in GFv (MSKFv)
 552 and GFu (MSKFu) for December 2015.

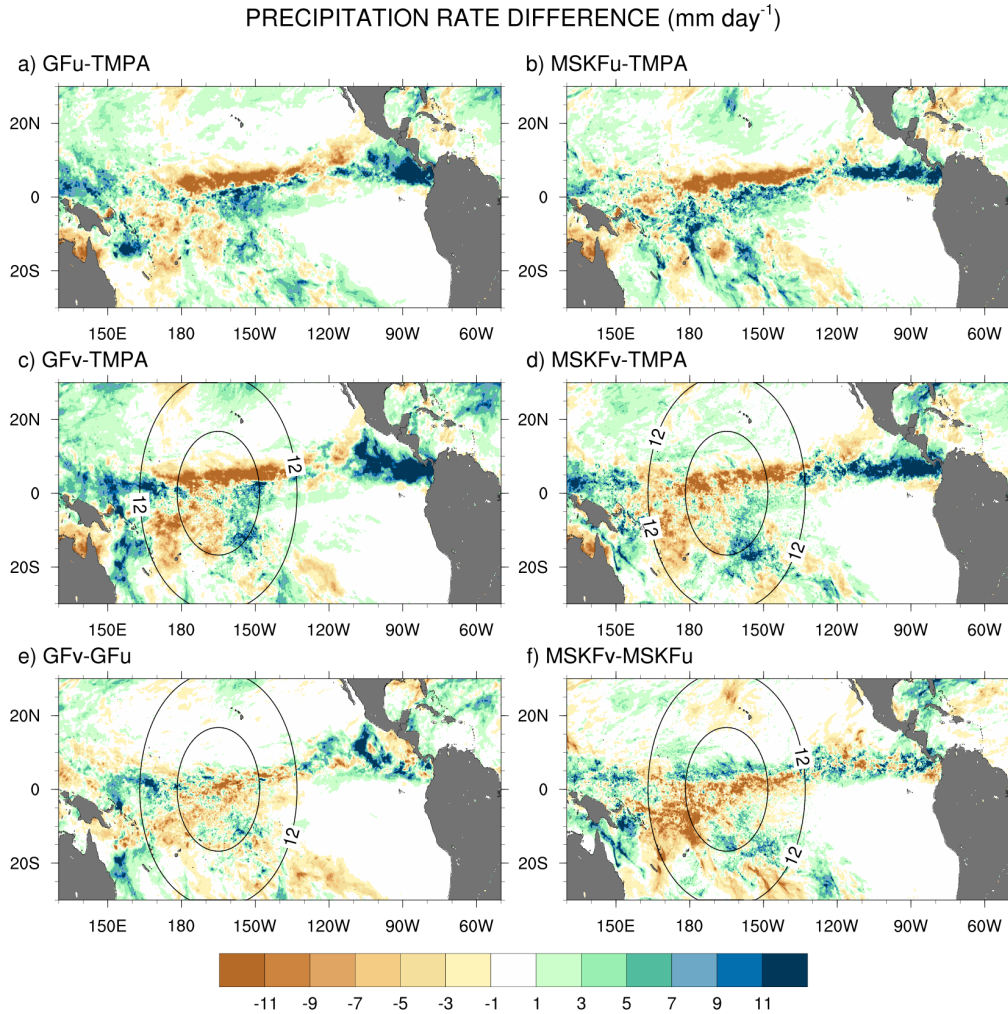
553 The simulated total precipitation rate can be compared to observed TMPA precipitation using Figs. 9 and 10
 554 which show the precipitation rates and differences between simulated and observed precipitation rates, respectively.
 555 Areas of maximum satellite-retrieved precipitation are found over the ITCZ between 130°W and the dateline (Fig.
 556 9.a). Observed precipitation decreases over the warm pool west of the dateline and decreases strongly over the Tropical
 557 Eastern Pacific (between 80°W and 120°W) and the SPCZ. The four simulations overestimate precipitation in the
 558 Tropical Eastern Pacific between 80°W and 120°W (Figs. 9.b-e) with biases in excess of 11 mm day⁻¹ (Figs. 10.a-d).
 559 The four simulations also overestimate precipitation between 130°E and 160°E, or west of the refined area, with biases
 560 about as large as those seen east of the refined area, except for MSKFu. The uniform-grid results (Figs. 9.b-c) display
 561 the highest precipitation rates over the area of warmest SSTs where we expect deepest convection to occur and are in
 562 reasonable agreement with TMPA data. However, GFu and MSKFu locate the ITCZ south of its observed location
 563 (Figs. 10.a-b), producing a positive bias straddling the Equator and a negative bias north of the Equator. The scale-
 564 aware dependence of deep convection in GF leads to decreased total precipitation in GFv compared to GFu over the
 565 entire refined area (Fig. 10.e). In contrast, Fig. 10.f shows that while the scale-aware dependence in MSKF leads to

566 decreased precipitation in MSKFv over a major fraction of the refined area, it also leads to an improved location of
 567 the simulated ITCZ, as evidenced by increased precipitation north of the Equator.



568
 569 **Figure 9:** Monthly-mean total precipitation rate over the Tropical Pacific Ocean from TMPA data (top panel) and simulated with
 570 GFu and MSKFu (middle panels) and GFv and MSKFv (bottom panels) for December 2015.

571 Table 3 summarizes the area-mean monthly-mean convective, grid-scale, and total simulated and observed TMPA
 572 precipitation rates over the REFINED and EAST areas. Over the two areas, the simulated total precipitation is about
 573 the same for all four experiments but is underestimated (overestimated) relative to TMPA data over the REFINED
 574 (EAST) areas, respectively. Over the REFINED area, total precipitation decreases by 2.1 mm day⁻¹ between GFu and
 575 GFv and 2.3 mm day⁻¹ between MSKFu and MSKFv, highlighting a near-equal compensation between decreased deep
 576 convective and increased grid-scale precipitation over the most refined area of the mesh. Over the EAST area, total
 577 precipitation increases by 2.7 mm day⁻¹ between GFu and GFv resulting from a 5.3 (2.6) mm day⁻¹ increase (decrease)
 578 in convective (grid-scale) precipitation. In contrast, total precipitation increases by 1.2 mm day⁻¹ between MSKFu and
 579 MSKFv resulting from a 0.5 (0.6) mm day⁻¹ increase in convective (grid-scale) precipitation. The large (small) increase
 580 in convective precipitation in GFv (MSKFv) over the coarse areas east (and west) of the refined area highlights distinct
 581 upscaling effect of the refined area on the coarse area of the mesh between GFv and MSKFv.



582
 583 **Figure 10:** Monthly-mean precipitation rate difference over the Tropical Pacific Ocean between GFu (MSKFu) and TMPA data
 584 (top panels), GFv (MSKFv) and TMPA data (middle panels), and between GFv (MSKFv) and GFu (MSKFu) (bottom panels) for
 585 December 2015.

586 In summary, the scale dependence of convection in GF and MSKF produces the same partitioning between
 587 convective and grid-scale precipitation inside the refined area or decreased convective and compensating increased
 588 grid-scale precipitation as horizontal resolution increases. The upscaling impact on convective and grid-scale
 589 precipitation varies between GF and MSKF. As seen in Fig. 8 and Table 3, convective precipitation increases strongly
 590 over the warm pool and Eastern Pacific starting across the transition zones east and west of the refined area in GFv.
 591 In contrast, while the parameterization of the scale dependence of deep convection in MSKF produces a stronger
 592 decrease in convective precipitation in MSKFv than GFv, it produces a smoother transition in convective precipitation
 593 and decreased upscaling effect as spatial resolution reaches 30 km.

	CONVECTIVE (mm day ⁻¹)		GRID-SCALE (mm day ⁻¹)		TOTAL (mm day ⁻¹)	
	REFINED	EAST	REFINED	EAST	REFINED	EAST
GFu	10.0	8.7	6.1	3.7	16.1	12.4
GFv	1.9	14.0	12.1	1.1	14.0	15.1
MSKFu	10.9	10.6	4.9	4.8	15.8	15.5
MSKFv	1.7	11.1	11.8	5.4	13.5	16.5
TMPA					20.7	7.3

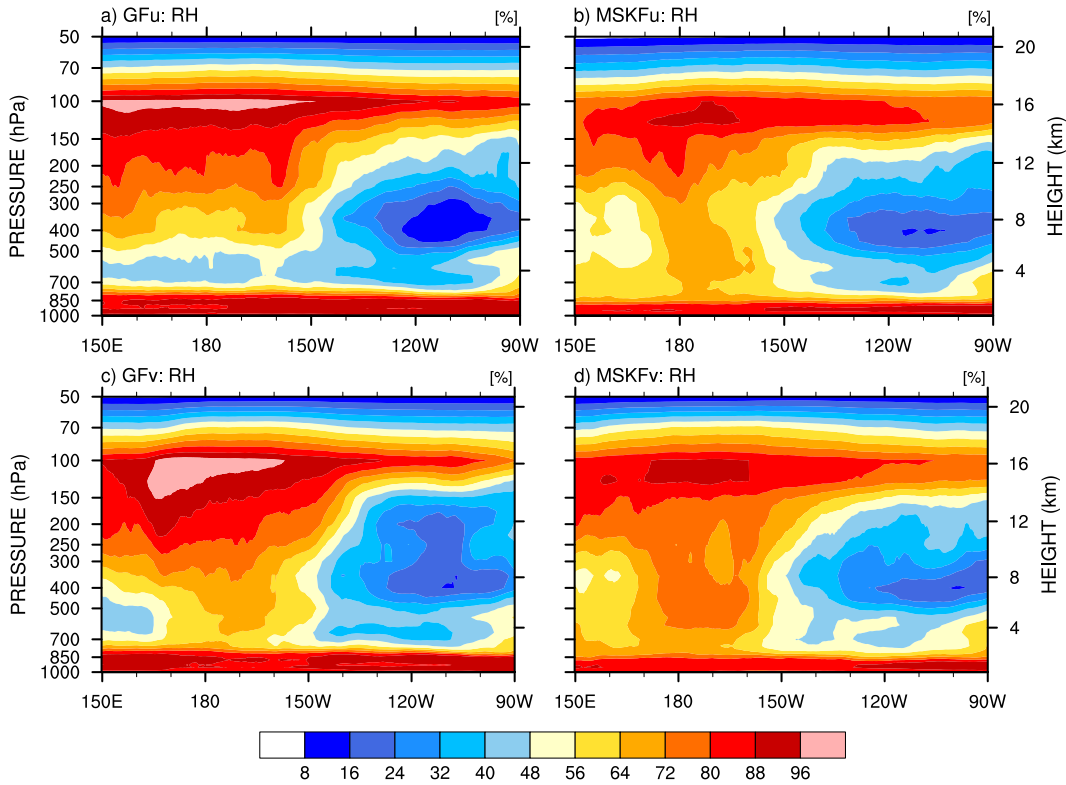
595 **Table 3:** Area-averaged convective, grid-scale, and total precipitation rates over the same areas as those described for Table 2. The
596 REFINED and EAST areas are shown in Figure 9.a.

597 **5 Simulated relative humidity and simulated versus satellite-retrieved LWP and IWP**

598 **5.1 Relative humidity**

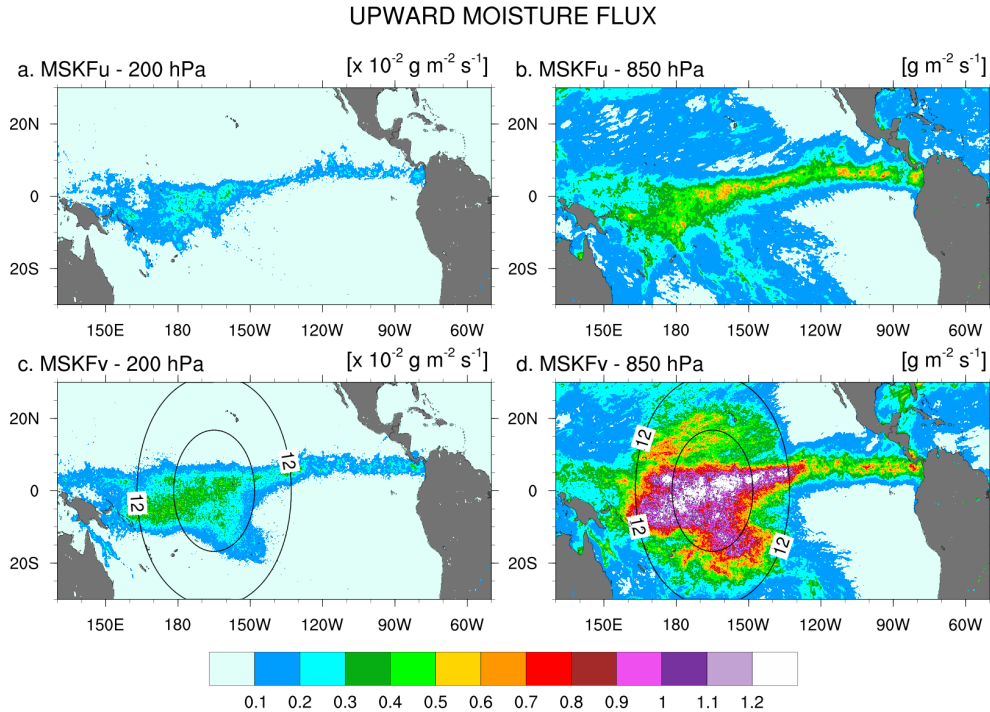
599 One effect of local mesh refinement is the decreased contribution of parameterized convection compensated by
600 increased contribution of grid-scale cloud microphysics to condensation processes and cloud formation with
601 increasing spatial resolution. Therefore, prior to comparing the simulated LWP and IWP against SSF data, we first
602 investigate differences in relative humidity (RH) between our uniform- and variable-resolution experiments. Figure
603 11 displays the monthly-mean longitude-pressure cross sections of RH latitudinally-averaged between 5°S and 5°N.
604 East of 150°W over the Tropical Eastern Pacific, the four experiments display similar vertical distributions of RH,
605 with relatively lower RH between 700 hPa and 150 hPa and higher RH in the PBL below 700 hPa and in the upper-
606 troposphere above 150 hPa. All four experiments show significant increase in RH west of 150°W across the entire
607 troposphere, over the warm pool where the warmest SSTs are seen (Fig. 2.a) and deepest convective updrafts are
608 formed. Comparing GFu against MSKFu over the warm pool shows that GF has stronger drying than MSKF in the
609 lower troposphere, leading to a lower RH between 850 hPa and 300 hPa in GFu than MSKFu. In addition, GF produces
610 stronger moistening than MSKF in the upper troposphere leading to a higher RH between 300 hPa and 100 hPa in
611 GFu than MSKFu. As seen in the bottom panels of Fig. 11, reducing parameterized deep convection while enhancing
612 grid-scale cloud microphysics produces a higher RH over the refined area in GFv and MSKFv, but without
613 significantly modifying RH over the coarse area of the mesh. Variations in the vertical distribution of RH at pressures
614 less than 400 hPa are more pronounced between GFu and GFv than between MSKFv and MSKFu. Because the cloud
615 fraction (CF) is a function of RH, as described in Xu and Randall (1996; Eq. 1), there is a strong relationship between
616 the longitude-pressure cross sections of RH and CF, as seen in Fig. S2 (see supplemental figures). The highest CF
617 coincide with the highest RH at about 100 hPa over the warm pool in all four experiments. As for RH, GFu and GFv
618 display higher and lower values of CF than MSKFu and MSKFv in the upper and lower troposphere. The top and
619 bottom panels of Fig. S3 show differences in RH and CF between GFv and GFu, and between MSKFv and MSKFu.
620 One notable difference is a stronger increase in upper-tropospheric clouds between MSKFu and MSKFv than between

621 GFv and GFu, particularly over the refined area of the mesh. While increased grid-scale condensation over the refined
 622 area impacts the entire troposphere in GFv, it more strongly affects the upper-troposphere in MSKFv.



623
 624 **Figure 11:** Longitude versus pressure cross-section of latitudinally-averaged (between 5°S and 5°N) relative humidity (RH) across
 625 the Tropical Pacific Ocean simulated in GFu and MSKFu (top panels) and GFu and GFv (bottom panels) for December 2015.

626 To explain the change in RH over the refined area between the uniform- and variable-resolution experiments, we
 627 compare the monthly-mean upward moisture flux at 850 hPa and 200 hPa between MSKFu and MSKFv over the
 628 Tropical Eastern Pacific (Fig. 12). There is a significant decrease in the upward moisture flux between 850 hPa and
 629 200 hPa in conjunction with decreased specific humidity with height in MSKFu and MSKFv (Fig. 11). As seen in the
 630 top panels of Fig. 12, MSKFu yields highest values of the upward moisture flux along the ITCZ and over the warm
 631 pool in association with parameterized deep convection. Outside the ITCZ and warm pool, lower values of the upward
 632 moisture flux at 850 hPa result because of reduced deep convection in conjunction with shallow convection, as seen
 633 over the SPCZ. At increased spatial resolution, convective processes transition from being parameterized to resolved,
 634 producing larger grid-scale vertical velocities, stronger upward moisture flux, and increased grid-scale condensation
 635 through the entire troposphere over the refined area of the mesh. Comparing the bottom versus top panels of Fig. 12
 636 outlines the intensification of vertical moisture transport at both pressure levels over the refined area, leading to the
 637 increased relative humidity with increased spatial resolutions shown in Fig. 11.

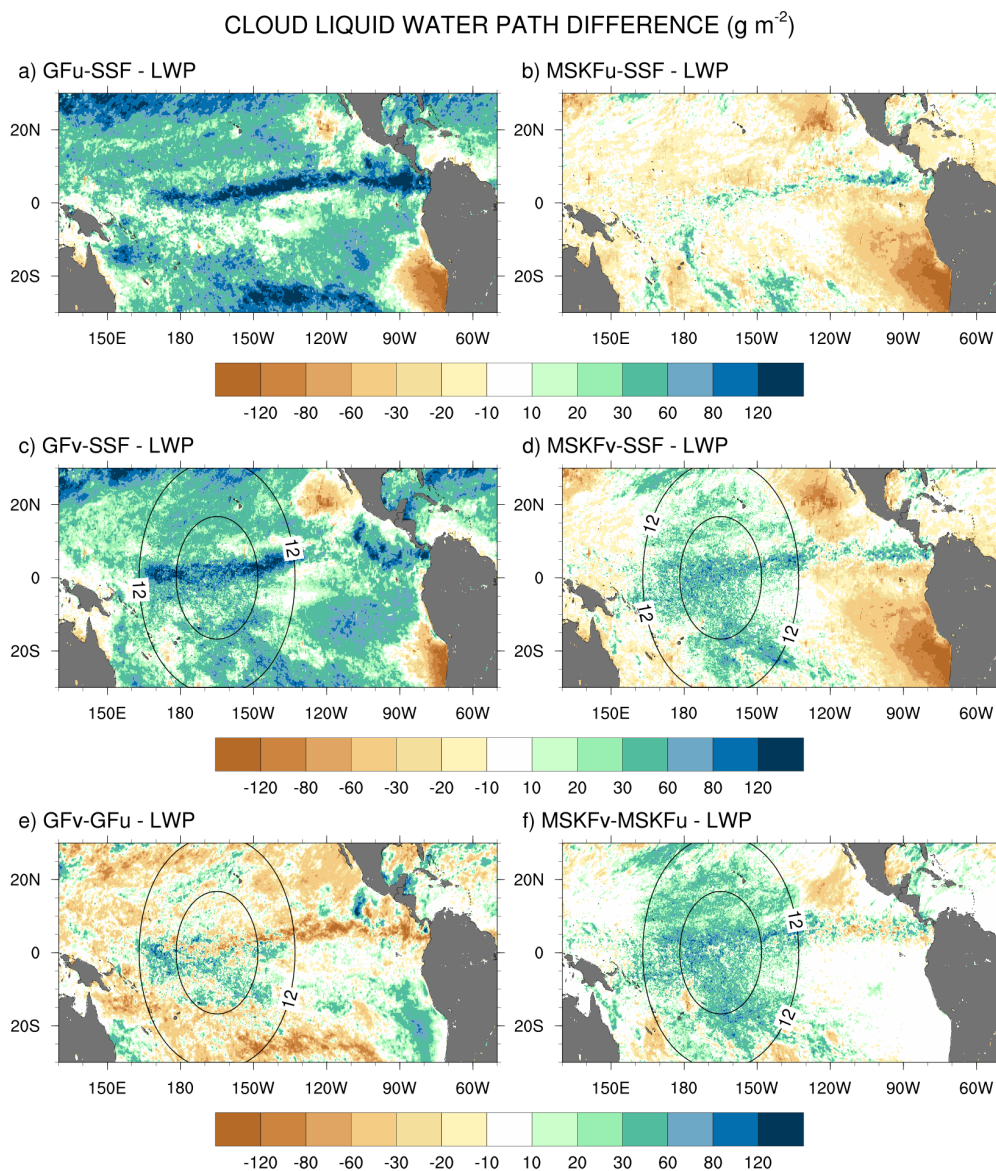


638
 639 **Figure 12:** 200 hPa (left panels) and 850 hPa (right panels) monthly-mean upward moisture flux simulated with MSKF over the
 640 Tropical Pacific Ocean for December 2015. Top panels are for MSKFu and bottom panels are for MSKFv. Note the 1×10^{-2} scaling
 641 between 200 hPa and 850 hPa.

642 **5.2 Liquid Water Path (LWP)**

643 Figure 13 displays difference maps between the simulated and satellite-derived LWP, and between GFv (MSKFv)
 644 and GFu (MSKFu). In Fig. 13, the simulated LWP is calculated using only the grid-scale cloud liquid water mixing
 645 ratio from THOM. Separate analyses would show that adding the prognostic grid-scale rain mixing ratio to the
 646 simulated LWP further increases biases when compared against the SSF LWP (not shown for brevity). We also do
 647 not include the contribution of the convective cloud liquid water mixing ratio to the LWP which is small compared to
 648 that from the grid-scale cloud microphysics. Figure 13 highlights that GFu strongly overestimates the LWP over the
 649 ITCZ, and between 20°N (20°S) and the northern (southern) limits of our analysis. As seen in Fig. 6, GFu attempts to
 650 form low-level boundary layer clouds off the coast of Peru but these clouds form too far west from the coast when
 651 compared against observations. This same bias is depicted in Fig 13.a since these low-level boundary layer clouds are
 652 characterized by high LWP. In Fig. 13.b, decreased bias between the MSKFu and SSF LWP reflects that the LWP is
 653 strongly decreased in MSKFu compared to GFu, outside of the areas of low-level boundary layer clouds. If we set
 654 aside that MSKFu is unable to simulate low-level clouds off the Baja Peninsula and coast of Peru, the magnitude and
 655 regional patterns of the LWP simulated in MSKFu is in fairly good agreement with the SSF LWP. Because MSKF
 656 does not allow deep and shallow convection to coexist within the same grid-cell and deep convection dominates
 657 shallow convection over the ITCZ and warm pool, we suggest that detrained cloud water from deep convection as a
 658 source to grid-scale microphysics contributes a major part to the LWP produced by MSKFu. The bottom panels of
 659 Fig. 13 reveal that the mesh refinement impacts the LWP simulated with MSKF more effectively than that simulated

660 with GF inside the refined area. This result is in agreement with the stronger increase in RH between MSKFu and
 661 MSKFv than between GFu and GFv at lower levels. MSKFv yields an increased LWP relative to MSKFu over the
 662 entire refined area (Fig. 13.f). MSKFv also has increased LWP compared to MSKFu over the coarse area, but not as
 663 large as that seen over the refined area. Figure 13.e shows that the LWP differences do not have a strong positive or
 664 negative trend inside the refined area, due to the fact that GF allows deep and shallow convection to coexist within
 665 the same grid-cell of deepest convective activity, mainly over the ITCZ and warm pool, and shallow convection does
 666 not account for variations in horizontal grid-spacing. Over the coarse area, an obvious decrease in the LWP between
 667 GFv and GFu is seen over the ITCZ in the Tropical Eastern Pacific as well as along the southern boundary of our
 668 analysis.

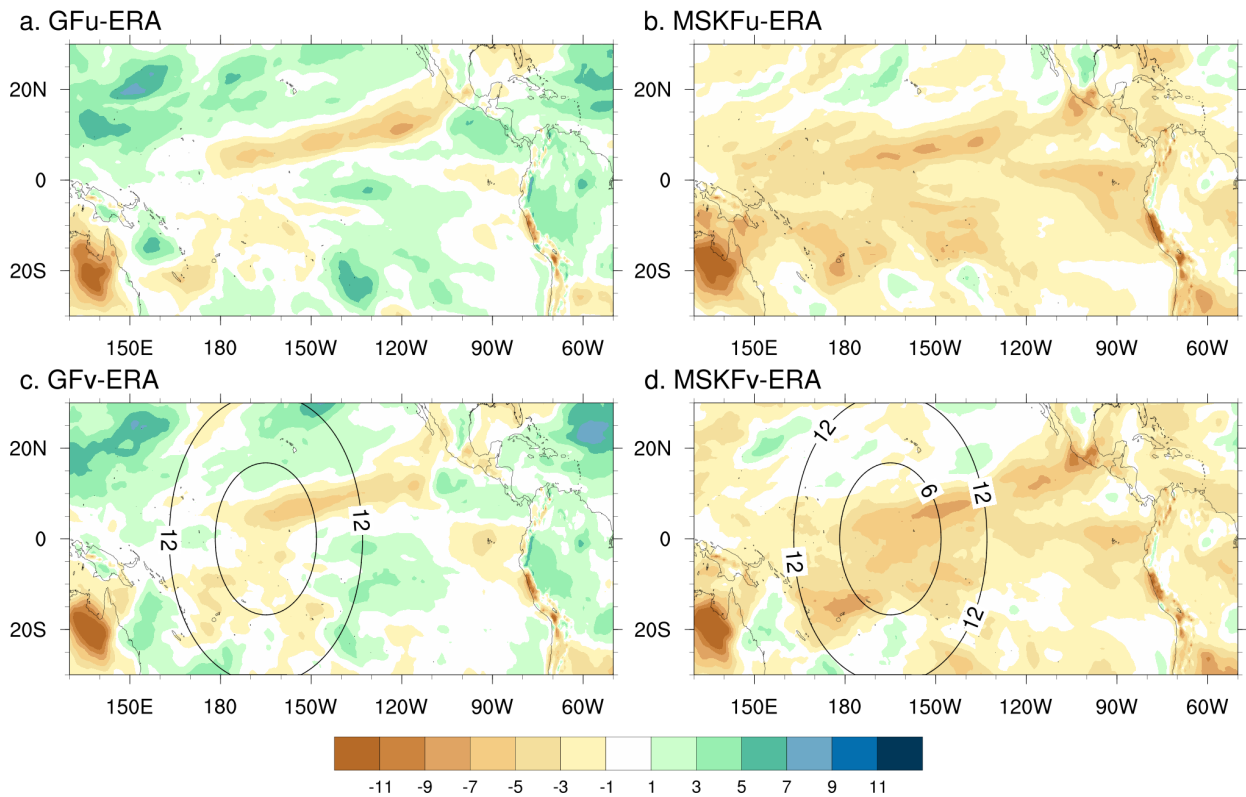


669
 670 **Figure 13:** Monthly-mean cloud liquid water path (LWP) difference over the Tropical Pacific Ocean between GFu (MSKFu) and
 671 SSF data (top panels), GFv (MSKFv) and SSF data (middle panels), and monthly-mean LWP difference between GFv (MSKFv)
 672 and GFu (MSKFu) (bottom panels) for December 2015.

673 In order to investigate the reasons why the LWP simulated in GFu strongly exceeds that from the SSF products
674 and MSKFu, we calculate the monthly-mean LWP produced in grid-cells with incidence of deep convection, shallow
675 convection, and no convection, using LWP hourly outputs from GFu. Separate maps show that a major fraction of the
676 LWP over convectively active regions such as the ITCZ is actually produced at times when no convection is active or
677 when only shallow convection is triggered (not shown for brevity). In GF, and in contrast to deep convection, shallow
678 convection detrains total water as a source of grid-scale water vapor instead of detraining water vapor, cloud liquid
679 and ice water, separately. Because the detrained total water is treated as a source of water vapor, supersaturation
680 conditions are more likely to persist and later removed by grid-scale condensation. In contrast, detrainment from deep
681 convective updrafts acts as a source of liquid water if temperatures are warmer than 258 K. Deep convection in
682 conjunction with grid-scale condensation contributes the least to the LWP because updrafts are taller and their cloud-
683 top temperatures colder than those from shallow convection, leading to condensation and deposition to occur at levels
684 where temperatures are colder than 258 K, and where ice phase processes dominate.

685 The impact of more active shallow convection in GFu (GFv) than in MSKFu (MSKFv) is analyzed using Fig. 14
686 which shows differences in the monthly-mean precipitable water below 700 hPa between our experiments and ERA-
687 Interim reanalyses. Because varying horizontal resolution does not affect shallow convection, GFv (MSKFv) displays
688 similar biases as GFu (MSKFu) over the entire analysis domain, including the refined area. Comparing the left versus
689 right panels of Figure 14 reveals that the precipitable water simulated in GFu (GFv) displays a positive bias whereas
690 that simulated in MSKFu (MSKFv) displays a negative bias in the lower troposphere relative to ERA-Interim data,
691 mainly over areas of shallow convection. In GF, the abundance of shallow convection (Figure 6.a, Figure 6.c)
692 associated with detrained total water acting as a source of grid-scale water vapor promotes the lower troposphere to
693 stay more humid and cloud liquid water to form more often than actually observed (Figure 13.a, Figure 13.c), north
694 and south of the ITCZ and warm pool. In MSKF, while shallow convection is as widespread over the Tropical Pacific
695 Ocean as in GF, it cannot act as a major source of detrained total water to the grid-scale microphysics because it is not
696 triggered as often as deep convection. In addition, because MSKF partitions detrained water into water vapor, cloud
697 water, cloud ice, rain, and snow, instead of detraining total water in the form of water vapor as in GF, the amounts of
698 available water vapor and cloud liquid water are reduced relative to GF.

PRECIPITABLE WATER BELOW 700 hPa (kg m^{-2})



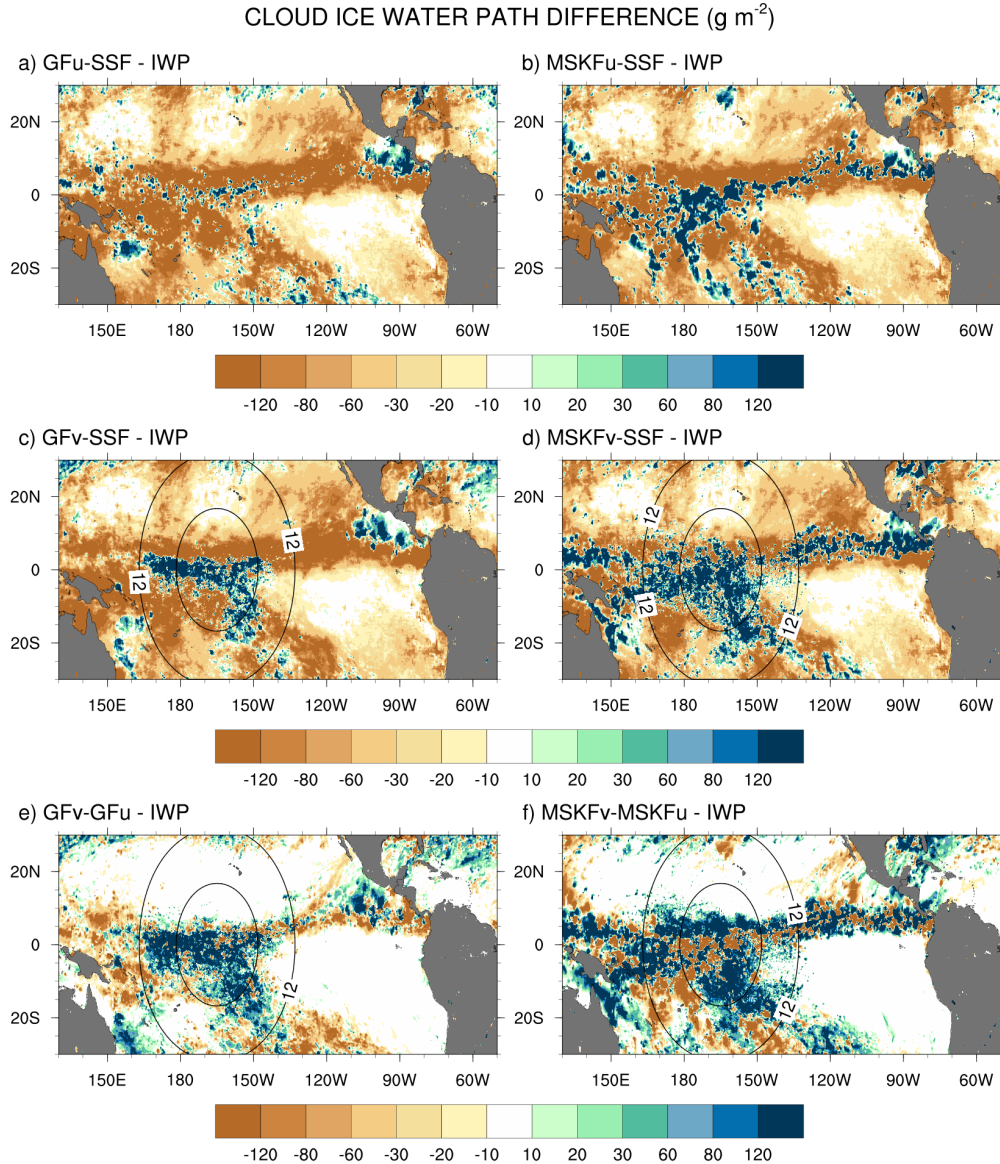
699

700 **Figure 14:** Monthly-mean difference between the simulated and ERA-Interim precipitable water below 700 hPa over the Tropical
701 Pacific Ocean for December 2015.

702 **5.3 Ice Water Path (IWP)**

703 Because MODIS is relatively insensitive to precipitation, the simulated IWP should comprise cloud ice, snow,
704 and graupel. Because graupel contributes a minor part to the IWP relative to cloud ice and snow and our results
705 highlight strong biases against SSF data, we do not include graupel in our computation of the simulated IWP. It is also
706 important to note that because THOM has the propensity to rapidly convert cloud ice to snow (Thompson et al. 2016),
707 most of the IWP is in the form of snow which falls at higher speeds than cloud ice, enhancing the depth of ice clouds.
708 Lastly, the middle panels of Fig. 5 show that our gridding of the IWP orbital data produce increased monthly mean
709 IWP than the official SSF1deg product. This result implies that biases between the simulated and satellite-derived
710 IWP will be underestimated when using our SSF $0.2^\circ \times 0.2^\circ$ IWP data. Figure 15 shows difference maps between the
711 simulated and satellite-derived IWP, and between GFv (MSKFv) and GFu (MSKFu). When compared against the SSF
712 IWP, GFu is the only experiment that mostly underestimates the IWP along the ITCZ and warm pool whereas GFv
713 yields a strong increase in the IWP over the refined area of the mesh relative to GFu. Both GFu and GFv overestimate
714 the IWP along the west coast of Central America, as they did for the LWP and precipitation. Comparing MSKFu
715 (MSKFv) against GFu (GFv) shows that MSKF leads to increased positive biases in the IWP compared to GF over

716 the entire ITCZ and warm pool. Increased convective detrainment of cloud ice as a source of grid-scale cloud ice to
 717 THOM in MSKF than in GFv, because partitioning between cloud liquid and ice water starts at warmer temperatures,
 718 may be responsible to the increased IWP. The bottom panels of Figure 15 reveal that increasing spatial resolution
 719 worsens the simulated IWP compared to the SSF IWP over the refined area in GFv and MSKFv. As shown in Fig. 11,
 720 mesh refinement over the warm pool yields higher upper-tropospheric relative humidity leading to increased ice cloud
 721 microphysics. In contrast to GFv, MSKFv displays an increase in the IWP over the coarse area of the mesh, showing
 722 a stronger impact of the refined area on the coarse area of the mesh in MSKFv than GFv in the upper-troposphere.



723
 724 **Figure 15:** As Fig. 13, but for the cloud ice water path (IWP).

725 **5.4 TOA radiation budget**

726 Biases in the LWP and IWP introduce biases in the cloud fraction and cloud optical properties which in turn lead
 727 to biases in the simulated TOALW and TOASW compared to CERES-SSF data. Figures S4, S5, and S6 display the

728 monthly-mean CF, TOALW, and TOASW from SSF data for December 2015 and the differences between the model
729 results and observations. Focusing on areas of deep convection over the ITCZ and warm pool, all four simulations
730 overestimate CF with larger biases seen in the GF than the MSKF experiments, and larger biases seen in the variable-
731 resolution than the uniform-resolution experiments. All four simulations also overpredict CF along the west coast of
732 Central America while underpredicting CF over areas of stratiform clouds along the west coast of South America and
733 Baja Peninsula. The impact of CF biases is that all four experiments underestimate the size of the warm pool and
734 width of the ITCZ, leading the TOALW (TOASW) to be too high (low) over areas of deep convection. These
735 differences are clearly linked to the differences noted in the LWP and IWP between MPAS and SSF data.

736 **6 Discussion**

737 When running GFu (MSKFu) and GFv (MSKFv), we set the time-step to be as large as possible to reduce the
738 computational cost of the various experiments without compromising computational stability. Using decreased time-
739 steps between the quasi- and variable-resolution experiments from 150 s to 30 s implies that it is not possible to directly
740 compare the mean state of GFv (MSKFv) against that of GFu (MSKFu) in the coarse area of the variable-resolution
741 mesh, and upscale effects of local mesh refinement. This is in contrast to Sakaguchi et al. (2015) and Hagos et al.
742 (2013) who constrain the time-step to be the same at all horizontal scales, allowing their study to assess the upscale
743 effect of mesh refinement across the transition zones between the refined and coarse areas of the mesh, and far from
744 the refined mesh. In order to understand the increase in convective precipitation east and west of the transition zones
745 in GFv relative to GFu, we run GFu with the reduced 30 s time-step to quantify the dependence of convective
746 precipitation to the dynamic time-step. As seen in Fig. S7.a (S7.b), reducing the time-step from 150 s to 30 s strongly
747 increases convective precipitation over convectively active regions of the Tropical Pacific Ocean, highlighting the
748 sensitivity of GF to the time-step. Reducing the time-step in MSKFu yields convective precipitation differences that
749 are not as large as those seen in Fig. S7.b (not shown for brevity). Using the Community Atmosphere Model Version
750 4 (CAM4) with a T340 spectral truncation and a 5 min time-step, Williamson (2013) demonstrates the dependence of
751 the removal of supersaturation conditions to the shallow (30 min) and deep (1 h) convective time-scales. While it is
752 important to point out that the sensitivity studies discussed in Williamson (2013) depend on the CAM4 coupling
753 between the convective and grid-scale cloud parameterizations and the dynamical core, shorter convective time-scales
754 relative to the time-step yield faster removal of moist instabilities through vertical motions and condensation. In GF,
755 the time-scales used in the *AS* and *KF* closures are set to the dynamical time-step and 20 min, respectively. While the
756 contribution of the *KF* closure decreases by a factor of 5 in response to the decreased time-step, the contribution of
757 the *AS* closure is independent of the convective time-scale but will affect the cloud base mass flux through variations
758 in the cloud work function. In order to further understand the impact of the time-step on increased supersaturation and
759 convective precipitation in GF, a detailed analysis of the contributions of the dynamics and physics forcing on the *AS*
760 cloud work function in MPAS is needed. This is the object of future research.

761 7 Summary and future research

762 Uniform- and variable-resolution experiments with two scale-aware parameterizations of deep convection (GF
763 and MSKF) in MPAS yield significant biases between the simulated and satellite-derived monthly-mean precipitation
764 rates, LWP, IWP, and CF over the Tropical Pacific Ocean for December 2015. In turn, biases affect the cloud fraction
765 and optical properties producing significant differences in the TOALW and TOASW compared to CERES-SSF data.

766 Tropical precipitation simulated with uniform-resolution experiments is overestimated compared to TMPA, due
767 to subgrid-scale deep convection. Biases using GF are as large as those using MSKF, and result in part because the
768 simulated ITCZ is located south of its observed location. Variable-resolution experiments do not produce significant
769 improvement in simulating precipitation against TMPA. Inside the refined area, decreased convective precipitation
770 plus compensating increased grid-scale precipitation have the simulated total precipitation to exhibit similar biases
771 between the uniform- and variable-resolution experiments with GF and MSKF. One major difference in using GF
772 instead of MSKF is the strong upscaling effect of the refined mesh on the coarse mesh, producing a strong increase in
773 convective precipitation east and west of the refined mesh. Because deep convection does not exhibit similar behaviour
774 over the transition zone between the coarse and refined areas of the mesh in MSKF, we plan further to investigate this
775 difference in convective precipitation in terms of the size of convective updrafts as a function of horizontal resolution
776 and increased moistening of the lower troposphere from shallow convection.

777 Differences in the simulated LWP between the uniform- and variable-resolution experiments using GF and MSKF
778 and against the CERES-SSF LWP highlight the need to revise the treatment of shallow convection to improve warm-
779 phase clouds in both schemes. While experiments using MSKF yield the simulated LWP to be in reasonable agreement
780 against that from the CERES-SSF product, those using GF yield the simulated LWP to be strongly overestimated.
781 Analyses show that shallow convection and cloud microphysics processes explain most of the increased LWP in GFu
782 and GFv compared to MSKFu and MSKFv, and satellite-derived data. We plan to update the GF shallow convection
783 scheme with that implemented in version 4.1 of the Advanced Research Weather Forecast (WRF) model. Because the
784 updated scheme includes an improved cloud model that allows water vapor and cloud liquid water to detrain separately
785 and a fraction of condensed water to precipitate, we will focus on the impact of explicit detrainment of cloud liquid
786 water and precipitation from shallow convective updrafts on the simulated LWP in GF. Results show that MSKF
787 underestimates shallow convection, leading the troposphere below 700 hPa to be drier than actually observed. These
788 results imply that the shallow convection in MSKF needs to be updated or that a separate parameterization of shallow
789 convection needs to be used in addition to that in MSKF. Using the same parameterization of shallow convection, and
790 partitioning of the detrained condensed water between cloud liquid water and ice in GF and MSKF, will further provide
791 understanding in the partitioning of the LWP between subgrid-scale deep and shallow convection. Variable-resolution
792 experiments strongly overestimate the IWP compared to CERES-SSF data over the refined area of the mesh, leading
793 to strong biases in the cloud fraction, and TOA long- and short-wave radiation. Because subgrid-scale deep convection
794 is reduced at increased horizontal resolutions, grid-scale cloud microphysics contributes a major part to biases in the
795 simulated IWP.

796 Parameterizing the dependence of subgrid-scale deep convection as a function of horizontal resolution allows the
797 use of variable-resolution meshes spanning between hydrostatic and nonhydrostatic scales within a global framework

798 for regional NWP and climate experiments. Although deep convection is not fully explicitly resolved over the refined
799 area of the mesh in our variables-resolution experiments, it is substantially reduced relative to that over the coarse area
800 of the mesh, allowing to contrast the contribution of subgrid-scale convection and cloud microphysics processes. As
801 horizontal resolution increases from the coarse to refined area of the mesh, deep convection gradually transitions from
802 parameterized to resolved and cloud microphysics contribute a major part to moist processes over the refined mesh.
803 Shallow convection coupled with grid-scale microphysics contributes a major part to the low-level cloud liquid water
804 and mixed-phase clouds whereas grid-scale cloud microphysics contribute a major part to the formation of upper-
805 tropospheric ice clouds over the refined area. Our results show that mesh refinement does not systematically improve
806 precipitation and clouds over the Tropical Pacific Ocean as grid-scale condensation increases at increased resolutions.
807 As cloud microphysics processes drive the moisture budget over the refined area of the mesh, we propose to expand
808 this diagnostic study to a process study by further understanding the cloud microphysics processes that need to be
809 improved in order to reduce discrepancies between model and observations. In that vein, the recently developed MSKF
810 that includes a double moment microphysics (Glotfelty et al., 2019) would be useful in a future process study.

811
812

813 *Code and data availability:* The source code used to initialize and run our experiments is based on MPAS-v5.2 which
814 is freely available from <https://github.com/MPAS-Dev/MPAS-Model/releases/tag/v5.2>. Modifications to the original
815 source code and scripts to run the experiments are available from <https://doi.org/10.5281/zenodo.3515440> (Fowler,
816 2019) while initialization files, and outputs from the experiments are located on the NCAR Campaign Storage System.
817 These files can be made available by contacting the corresponding author. Examples of CERES SSF Aqua and Terra
818 orbital and gridded data, daily-mean and monthly-mean simulated diagnostics, and post-processing scripts are also
819 available from <https://doi.org/10.5281/zenodo.3515440> (Fowler, 2019).

820
821

822 *Author contributions:* LF developed all the modifications that were made to the MPAS-v5.2 released version and were
823 necessary to run the different experiments. KA made all the updates to the MultiScale Kain-Fritsch parameterization
824 of convection. LF and MB designed the experiments, and LF conducted and analyzed the simulations. LF prepared
825 the manuscript with contributions from all co-authors.

826
827

828 *Competing interests:* The authors declare that they have no conflict of interest.

829
830

831 *Acknowledgments:* This research is based upon work supported by the National Center for Atmospheric Research
832 which is a major facility sponsored by the National Science Foundation under Cooperative Agreement No. 1852977.
833 The authors thank Dr. Hugh Morrison for his careful review and constructive suggestions of the manuscript prior to
834 its submission. The authors thank two anonymous reviewers for their valuable comments and critics that helped

835 improve the clarity of the manuscript. The CERES-SSF data were obtained from the NASA Langley Research Center
836 Atmospheric Science Data Center. The TMPA data were acquired as part of the activities of NASA's Science Mission
837 Directorate and are archived and distributed by the Goddard Earth Sciences (GES) Data and Information Services
838 Center (DISC). We would like to acknowledge high-performance computing support from Cheyenne
839 (doi:10.5065/D6RX99hX) provided by NCAR's Computational and Information Systems Laboratory, sponsored by
840 the National Science Foundation. We acknowledge the use of the NCAR Command Language (Version 6.3.2)
841 [Software]. (2019). Boulder, Colorado: UCAR/NCAR/CISL/TDD. <http://dx.doi.org/10.5065/D6WD3XH5> for all
842 figures.

843

References

- 844 Alapaty, K., Herwehe, J.A., Otte, T.L., Nolte, C.G., Bullock, O.R., Ballard, M.S., Kain, J.S., and Dudhia, J.:
845 Introducing subgrid-scale cloud feedbacks to radiation for regional meteorological and climate modeling,
846 *Geophys. Res. Lett.*, 39, L24809, <https://doi.org/10.1029/2012GL054031>, 2012.
- 847 Alishouse, J.C., Snider, J.B., Westwater, E.R., Swift, C.T., Ruf, C.S., Vongsathron, S.A., and Ferraro, R.R.:
848 Determination of cloud liquid water content using the SSM/I, *IEEE T. Geosci. Remote*, 28, 817-822,
849 <https://doi.org/10.1109/36.58968>, 1990.
- 850 Arakawa, A., and Schubert, W.H.: Interaction of a cumulus cloud ensemble with the large-scale environment, Part I,
851 *J. Atmos. Sci.*, 31, 674-701, [https://doi.org/10.1175/1520-0469\(1974\)031<0674:IOACCE>2.0.CO;2](https://doi.org/10.1175/1520-0469(1974)031<0674:IOACCE>2.0.CO;2), 1974.
- 852 Arakawa, A., and Wu, C.-M.: A unified representation of deep moist convection in numerical modeling of the
853 atmosphere. Part I, *J. Atmos. Sci.*, 70, 1977-1992, <https://doi.org/10.1175/JAS-D-12-0330.1>, 2013.
- 854 Bechtold, P., Bazile, E., Guichard, F., Mascart, P., and Richard, E.: A mass-flux convection scheme for regional and
855 global models, *Q. J. Roy. Meteor. Soc.*, 130, 3139-3172, <https://doi.org/10.1002/qj.49712757309>, 2001.
- 856 Bechtold, P., Köhler, M., Jung, T., Doblas-Reyes, F., Leutbecher, M., Rodwell, M. J., Vitart, F., and Balsamo, G.:
857 Advances in simulating atmospheric variability with the ECMWF model: From synoptic to decadal time-scales,
858 *Q. J. Roy. Meteor. Soc.*, 134, 1337-1351, <https://doi.org/10.1002/qj.289>, 2008.
- 859 Brown, J.M.: Mesoscale unsaturated downdrafts driven by rainfall evaporation: A numerical study, *J. Atmos. Sci.*, 36,
860 313-338, [https://doi.org/10.1175/1520-0469\(1979\)036<0313:MUDDBR>2.0.CO;2](https://doi.org/10.1175/1520-0469(1979)036<0313:MUDDBR>2.0.CO;2), 1979.
- 861 Chen, F., and Dudhia, J.: Coupling an advanced land surface-hydrology model with the Penn State-NCAR MM5
862 modeling system. Part I: Model implementation and sensitivity, *Mon. Weather Rev.*, 129, 569-585,
863 [https://doi.org/10.1175/1520-0493\(2001\)129<0569:CAALSH>2.0.CO;2](https://doi.org/10.1175/1520-0493(2001)129<0569:CAALSH>2.0.CO;2), 2001.
- 864 Dee, D.P., and 35 co-authors: The ERA-Interim reanalysis: configuration and performance of the data assimilation
865 system, *Q. J. Roy. Meteor. Soc.*, 137, 553-597, <https://doi.org/10.1002/qj.828>, 2011.
- 866 Dolinar, E.K., Dong, X., Xi, B., Jiang, J.H., and Su, H.: Evaluation of CMIP5 simulated clouds and TOA radiation
867 budgets using NASA satellite observations, *Clim. Dynam.*, 44, 2229-2247, [https://doi.org/10.1007/s00382-014-](https://doi.org/10.1007/s00382-014-2158-9)
868 [2158-9](https://doi.org/10.1007/s00382-014-2158-9), 2015.
- 869 Fowler, L.D., Skamarock, W.C., Grell, G.A., Freitas, S.R., and Duda, M.G.: Analyzing the Grell-Freitas convection
870 scheme from hydrostatic to nonhydrostatic scales within a global model, *Mon. Weather Rev.*, 144, 2285-2306,
871 <https://doi.org/10.1175/MWR-D-15-0311.1>, 2016.
- 872 Frank, W.M., and Cohen, C.: Simulation of tropical convective systems. Part I: A cumulus parameterization, *J. Atmos.*
873 *Sci.*, 44, 3787-3799, [https://doi.org/10.1175/1520-0469\(1987\)044<3787:SOTCSP>2.0.CO;2](https://doi.org/10.1175/1520-0469(1987)044<3787:SOTCSP>2.0.CO;2), 1987.

874 Fritsch, J.M., and Chappell, C.F.: Numerical prediction of convectively driven mesoscale pressure systems. Part I:
875 Convective parameterization, *J. Atmos. Sci.*, 37, 1722–1733, [https://doi.org/10.1175/1520-0469\(1980\)037<1722:NPOCDM>2.0.CO;2](https://doi.org/10.1175/1520-0469(1980)037<1722:NPOCDM>2.0.CO;2), 1980.

877 Fowler, L.D.: experimentsMPAS-v5.2, Zenodo, <https://doi.org/10.5281/zenodo.3515440>, 2019.

878 Geier, E.B., Green, R.N., Kratz, D.P., Minnis, P., Miller, W.F., Nolan, S.K., and Franklin, C.B.: Clouds and the Earth’s
879 Radiant Energy System (CERES) data management system. Single Satellite Footprint TOA/Surface Fluxes and
880 Clouds (SSF) collection document. Release 2, Version 1, 243 pp, 2003.

881 Giorgetta, M.A., Brokopf, R., Crueger, T., Esch, M., Fiedler, S., Helmert, J., Hohenegger, C., Kornblueh, L., Köhler,
882 M., Manzini, E., Mauritsen, T., Nam, C., Raddatz, T., Rast, S., Reinert, D., Sakradzija, M., Schmidt, H., Schneck,
883 R., Schnur, R., Silvers, L., Wan, H., Zängl, G., and Stevens, B: ICON-A, the atmosphere component of the ICON
884 Earth System Model: I. Model description, *J. Adv. Model. Earth Sy.*10, 1613-1637,
885 <https://doi.org/10.1029/2017MS001242>, 2018.

886 Glotfelty, T., Alapaty, K., He, J., Hawbecker, P., Song, X., and Zhang, G.: The Weather Research and Forecasting
887 Model with aerosol cloud-interactions (WRF-ACI): Development, evaluation, and initial applications, *Mon. Wea.*
888 *Rev.*, 147, 1491-1511, <https://doi.org/10.1175/MWR-D-18-0267.1>, 2019.

889 Greenwald, T.J., Stephens, G.L., Vonder Haar, T.H., and Jackson, D.L.: A physical retrieval of cloud liquid water
890 over global oceans using special sensor microwave/imager (SSM/I) observations, *J. Geophys. Res.*, 98, 18471-
891 18488, <https://doi.org/10.1029/93JD00339>, 1993.

892 Grell, G.A.: Prognostic evaluation of assumptions uses by cumulus parameterizations, *Mon. Weather Rev.*, 121, 764-
893 787, [https://doi.org/10.1175/1520-0493\(1993\)121<0764:PEOAUB>2.0.CO;2](https://doi.org/10.1175/1520-0493(1993)121<0764:PEOAUB>2.0.CO;2), 1993.

894 Grell, G.A., and Dévényi, D.: A generalized approach to parameterizing convection combining ensemble and data
895 assimilation techniques, *Geophys. Res. Lett.*, 29, 38-1-38-4, <https://doi.org/10.1029/2002GL015311>, 2002.

896 Grell, G.A., and Freitas, S.R.: A scale and aerosol aware stochastic parameterization for weather and air quality
897 modeling, *Atmos. Chem. Phys.*, 14, 5233-5250, <https://doi.org/10.5194/acp-14-5233-2014>, 2014.

898 Guo, H., Golaz, J.-C., Donner, L., Wyman, B., Zhao, M., and Ginoux, P.: CLUBB as a unified cloud parameterization:
899 opportunities and challenges, *Geophys. Res. Lett.*, 42, 4540-4547, <https://doi.org/10.1002/2015GL063672>, 2015.

900 Hagos, S., Leung, L.R., Rauscher, S.A., and Ringler, T.: Error characteristics of two grid refinement approaches in
901 aquaplanet simulations: MPAS-A and WRF, *Mon. Wea. Rev.*, 141, 3022-3036, <https://doi.org/10.1175/MWR-D-12-00338.1>, 2013.

903 He, J., and Alapaty, K.: Precipitation partitioning in multiscale atmospheric simulations: Impacts of stability
904 restoration methods, *J. Geophys. Res.*, 123, 10185-10201, <https://doi.org/10.1029/2018JD028710>, 2018.

905 Herwehe, J.A., Alapaty, K., and Bullock Jr., O.R: Evaluation of developments toward a multi-scale Kain-Fritsch
906 parameterization in WRF. 2014 Community Modeling and Analysis System Conference, Chapel Hill, NC, EPA,
907 2014.

908 Hong, S.-Y., and Lim, J.-O: The WRF single moment 6-class microphysics scheme (WSM6), *J. Korean Meteor. Soc.*,
909 42, 129-151, 2006.

910 Hong, S.-Y., Choi, J., Chang, E.-C., Park, H., and Kim Y.-J.: Lower-tropospheric enhancement of gravity wave drag
911 in a global spectral atmospheric forecast model, *Weather Forecast*, 23, 523-531,
912 <https://doi.org/10.1175/2007WAF2007030.1>, 2008.

913 Huffman, G.J., Balvin, D.T., Nelkin, E.J., and Wolff, D.B.: The TRMM Multisatellite Precipitation Analysis (TMPA):
914 Quasi-global, multiyear, combined-sensor precipitation at fine scales, *J. Hydrometeorol.*, 8, 38-55,
915 <https://doi.org/10.1175/JHM560.1>, 2007.

916 Iacono, M. J., Mlawer, E. J., Clough, S. A., and Morcrette, J.-J.: Impact of an improved longwave radiation model,
917 RRTM, on the energy budget and thermodynamic properties of the NCAR Community Climate Model, CCM3,
918 *J. Geophys. Res.*, 105, 14 873–14 890, <https://doi.org/10.1029/2000JD900091>, 2000.

919 Jiang, J.H., Su, H., Zhai, C., Perun, V.S, Del Genio, A., Nazarenko, L.S., Donner, L.J., Horowitz, L., Seman, C., Cole,
920 J., Gettelman, A., Ringer, M.A., Rotstayn, L., Jeffrey, S., Wu, T., Brient, F., Dufresne, J.-L., Kawai, H., Koshiro,
921 T., Watanabe, M., L’Ecuyer, T.S., Volodin, E.M., Iversen, T., Drange, H., Mesquita, M.D.S., Read, W.G., Waters,
922 J.W., Tian, B., Teixeira, J., and Stephens, G.L.: Evaluation of cloud and water vapor simulations in CMIP5
923 climate models using NASA “A-Train” satellite observations, *J. Geophys. Res.*, 117, D14105,
924 <https://doi.org/10.1029/2011JD017237>, 2012.

925 Ju, L., Ringler, T., and Gunzburger, M.: Voronoi tessellations and their applications to climate and global modeling,
926 *Numerical Techniques for Global Atmospheric Models*, P. Lauritzen et al., Eds., Springer, 313-342, 2011.

927 Judt, F.: Atmospheric predictability of the tropics, middle latitudes, and polar regions explored through global storm-
928 resolving simulations, *J. Atmos. Sci.*, 77, 257-276, <https://doi.org/10.1175/JAS-D-19-0116.1>, 2020.

929 Kain, J.S.: The Kain-Fritsch parameterization: An update, *J. Appl. Meteorol.*, 43, 170-181,
930 [https://doi.org/10.1175/1520-0450\(2004\)043<0170:TKCPAU>2.0.CO;2](https://doi.org/10.1175/1520-0450(2004)043<0170:TKCPAU>2.0.CO;2), 2004.

931 Kain, J.S, and Fritsch, J.M.: A one-dimensional entraining/detraining plume model and its application in convective
932 parameterization, *J. Atmos. Sci.*, 47, 2784-2802, [https://doi.org/10.1175/1520-0469\(1990\)047<2784:AODEPM>2.0.CO;2](https://doi.org/10.1175/1520-0469(1990)047<2784:AODEPM>2.0.CO;2), 1990.

934 Kain, J.S., and Fritsch, J.M.: The role of convective “trigger function” in numerical forecasts of mesoscale convective
935 systems, *Meteorol. Atmos. Phys.*, 49, 93-106, <https://doi.org/10.1007/BF01025402>, 1992.

936 Kain, J.S., and Fritsch, J.M.: Convective parameterization for mesoscale models: The Kain-Fritsch scheme, *The*
937 *Representation of Cumulus Convection in Numerical Models*, Meteor. Mon., No. 24, American Meteorological
938 Society, Boston, MA, 165-170, https://doi.org/10.1007/978-1-935704-13-3_16, 1993.

939 Kay, J.E., Deser, C., Phillips, A., Mai, A., Hannary, C., Strand, G., Arblaster, J.M., Bates, S.C., Danabasoglu, G.,
940 Edwards, J., Holland, M., Kushner, P., Lamarque, J.-F., Lawrence, D., Lindsay, K., Middleton, A., Munoz, E.,
941 Neale, R., Oleson, K., Polvani, L., and Vertenstein, M.: The Community Earth System Model (CESM) large
942 ensemble project, *B. Am. Meteorol. Soc.*, 96, 1333-1349, <https://doi.org/10.1175/BAMS-D-13-00255.1>, 2015.

943 Kessler, E.: On the distribution and continuity of water substances in atmospheric circulation, *Meteor. Mon.*, No. 10,
944 American Meteorological Society, Boston, MA, 1-84, https://doi.org/10.1007/978-1-935704-36-2_1, 1969.

945 Klemp, J.B.: A terrain-following coordinate with smoothed coordinate surfaces, *Mon. Weather Rev.*, 139, 2163-2169,
946 <https://doi.org/10.1175/MWR-D-10-05046.1>, 2011

947 Klemp, J.B., Skamarock, W.C., and Dudhia, J.: Conservative split-explicit time integration methods for the
948 compressible nonhydrostatic equations, *Mon. Weather Rev.*, 135, 2897-2913,
949 <https://doi.org/10.1175/MWR3440.1>, 2007.

950 Krishnamurti, T.N., Low-Nam, S., and Pasch, R.: Cumulus parameterization and rainfall rates II, *Mon. Weather Rev.*,
951 111, 815-828, [https://doi.org/10.1175/1520-0493\(1983\)111<0815:CPARRI>2.0.CO;2](https://doi.org/10.1175/1520-0493(1983)111<0815:CPARRI>2.0.CO;2), 1983.

952 Li, J.-L., Waliser, D., Woods, C., Teixeira, J., Bacmeister, J., Chern, J., Shen, B.-W., Tompkins, A., Tao, W.-K., and
953 Köhler, M.: Comparisons of satellites liquid water estimates to ECMWF and GMAO analyses, 20th century IPCC
954 AR4 climate simulations and GCM simulations, *Geophys. Res. Lett.*, 35, L9710,
955 <https://doi.org/10.1029/2008GL035427>, 2008.

956 Li, J.-L., Waliser, D.E., Chen, W.-T., Guan, B., Kubar, T., Stephens, G., Ma, H.-Y., Deng, M., Donner, L., Seman,
957 C., and Horowitz, L.: An observational based evaluation of cloud ice water in CMIP3 and CMIP5 GCMs and
958 contemporary reanalyses using contemporary satellite data, *J. Geophys. Res.*, 117, D16105,
959 <https://doi.org/10.1029/2012JD017640>, 2012.

960 Li, J.-L., Lee, S., Ma, H.-Y., Stephens, G., and Guan, B.: Assessment of the cloud liquid water from climate models
961 and reanalysis using satellite observations, *Terr. Atmos. Ocean. Sci.*, 29(6), 653-678,
962 <https://doi.org/10.3319/TAO.2018.07.04.01>, 2018.

963 Mahoney, K.M.: The representation of cumulus convection in high-resolution simulations of the 2013 Colorado front
964 range flood, *Mon. Weather Rev.*, 144, 4265-4278, <https://doi.org/10.1175/MWR-D-16-0211.1>, 2016.

965 Meehl, G.A., Delworth, T.L., Latiff, M., McAveney, B., Mitchell, J.F.B., Stouffer, R.J., and Taylor, K.E.: The WCRP
966 CMIP3 multimodel dataset: A new era in climate change research, *B. Am. Meteorol. Soc.*, 88, 1383-1394,
967 <https://doi.org/10.1175/BAMS-88-9-1383>, 2007.

968 Minnis, P., and coauthors: CERES Edition-2 cloud property retrievals using TRMM VIRS and Terra and Aqua
969 MODIS data-Part I: Algorithms, *IEEE T. Geosci. Remote.*, Vol. 49, NO 11, 4374-4400,
970 <https://doi.org/10.1109/TGRS.2011.2144601>, 2011.

971 Minnis, P., Kratz, D.P., Coakley, J.J.A., King, M.D., Garber, D., Heck, P., Mayor, S., Young, D.F., and Arduini, R.:
972 Cloud optical property retrieval (Subsystem 4.3), in *Clouds and the Earth's Radiant Energy System (CERES)*

973 Algorithm Theoretical Basis Document, Vol III, Clouds and Radiance Inversions (Subsystem 4), NASA RP 1376,
974 edited by Science Team CERES, pp. 135-176, NASA, Washington D.C., 1995.

975 Mlawer, E. J., Taubman, S. J., Brown, P. D., Iacono, M. J., and Clough, S. A.: Radiative transfer for inhomogeneous
976 atmospheres: RRTM, a validated correlated-k model for the longwave, *J. Geophys. Res.*, 102, 16663–16682,
977 <https://doi.org/10.1029/97JD00237>, 1997.

978 Molod, A., Takacs, L., Suarez, M., Bacmeister, J., Song, I.-S., and Eichman, A.: The GEOS-5 atmospheric general
979 circulation model: Mean climate from MERRA to Fortuna, Technical Report Series on Global Modeling and
980 Assimilations, Vol. 28, 124 pp, 2012.

981 Moorthi, S., and Suarez, M.J.: Relaxed Arakawa-Schubert: a parameterization of moist convection for general
982 circulation models, *Mon. Wea. Rev.*, 210, 978-1002, [https://doi.org/10.1175/1520-
983 0493\(1992\)120<0978:RASAPO>2.0.CO;2](https://doi.org/10.1175/1520-0493(1992)120<0978:RASAPO>2.0.CO;2), 1992.

984 Nakanishi, M., and Niino, H.: Development of an improved turbulence closure model for the atmospheric boundary
985 layer, *J. Meteor. Soc. Japan*, 87, 895–912, <https://doi.org/10.2151/jmsj.87.895>, 2009.

986 Ogura, Y., and Cho, H.-R.: Diagnostic determination of cumulus cloud populations from observed large-scale
987 variables, *J. Atmos. Sci.*, 30, 1276-1286, [https://doi.org/10.1175/1520-
988 0469\(1973\)030<1276:DDOCCP>2.0.CO;2](https://doi.org/10.1175/1520-0469(1973)030<1276:DDOCCP>2.0.CO;2), 1973.

989 Olson, J.B., Kenyon, J.S., Angevine, W.M., Brown, J.M., Pagowski, M., and Suselj, K.: A description of the MYNN-
990 EDMF scheme and the coupling to other components in WRF-ARW, NOAA Technical Memorandum OAR GSD,
991 61, pp 37, 2019.

992 Platnick, S., King, M.D., Ackerman, S.A., Wenzel, W.P., Baum, B.A., Riedl, J.C., and Frey, R.A.: The MODIS cloud
993 products: Algorithms and examples from Terra, *IEEE T. Geosci. Remote*, 41, 459-473,
994 <https://doi.org/10.1109/TGRS.2002.808301>, 2003.

995 Qiao, F., and Liang, X-Z: Effects of cumulus parameterization closures on the simulations of summer precipitation
996 over the United States coastal oceans, *J. Adv. Model. Earth Sy.*, 8, 764-785,
997 <https://doi.org/10.1002/2015MS000621>, 2015.

998 Raymond, D.J.: Regulation of moist convection over the west Pacific warm pool, *J. Atmos. Sci.*, 52, 3945-3959,
999 [https://doi.org/10.1175/1520-0469\(1995\)052<3945:ROMCOT>2.0.CO;2](https://doi.org/10.1175/1520-0469(1995)052<3945:ROMCOT>2.0.CO;2), 1995.

1000 Sakaguchi, K., Leung, L.R., Zhao, C., Yang, Q., Lu, J., and Hagos, S.: Exploring a multiresolution approach using
1001 AMIP simulations, *J. Clim.*, 28, 5549-5574, <https://doi.org/10.1175/JCLI-D-14-00729.1>, 2015.

1002 Schwarz, C.S.: Medium-range convection-allowing ensemble forecasts with a variable-resolution global model, *Mon.
1003 Weather Rev.*, 147, 2997-3023, <https://doi.org/10.1175/MWR-D-18-0452.1>, 2019.

1004 Simpson, J., and Wiggert, V.: Models of precipitating cumulus towers, *Mon. Weather Rev.*, 97, 471-489,
1005 [https://doi.org/10.1175/1520-0493\(1969\)097<0471:MOPCT>2.3.CO;2](https://doi.org/10.1175/1520-0493(1969)097<0471:MOPCT>2.3.CO;2), 1969.

1006 Skamarock, W.C., and Gassmann, A.: Conservative transport schemes for spherical geodesic grids: High-order flux
1007 operators for ODE-based time integration, *Mon. Weather Rev.*, 139, 2962-2975, <https://doi.org/10.1175/MWR->
1008 [D-10-05056.1](https://doi.org/10.1175/MWR-D-10-05056.1), 2011.

1009 Skamarock, W.C., Klemp, J.B., Duda, M.G., Fowler, L.D., Park, S.-H., and Ringler, T.D.: A multiscale nonhydrostatic
1010 atmospheric model using Centroidal Voronoi tessellations and C-grid staggering, *Mon. Weather Rev.*, 140, 3090-
1011 3105, <https://doi.org/10.1175/MWR-D-11-00215.1>, 2012.

1012 Skamarock, W.C., and Coauthors: A description of the Advanced Research WRF version 3, NCAR Tech. Note
1013 NCAR/TN-475+STR, 113 pp, 2008.

1014 Smagorinsky, J.: General circulation experiments with the primitive equations. I. The basic experiment, *Mon. Weather*
1015 *Rev.*, 91, 99-164, [https://doi.org/10.1175/1520-0493\(1963\)091<0099:GCEWTP>2.3.CO;2](https://doi.org/10.1175/1520-0493(1963)091<0099:GCEWTP>2.3.CO;2), 1963.

1016 Stanfield, R.E., Dong, X., Xi, B., Del Genio, A.D., Minnis, P., Doelling, D., and Loeb, N.: Assessment of NASA
1017 GISS CMIP5 and Post-CMIP5 simulated clouds and TOA radiation budgets using satellite observations. Part II:
1018 TOA radiation budget and CREs, *J. Climate*, 28, 1842-1863, <https://doi.org/10.1175/JCLI-D-14-00249.1>, 2015.

1019 Stephens, G.L., and Kummerow, C.D.: The remote sensing of clouds and precipitation from space: A review, *J. Atmos.*
1020 *Sci.*, 64, 3742-3765, <https://doi.org/10.1175/2006JAS2375.1>, 2007.

1021 Stephens, G.L., Vane, D.G., Boain, R.J., Mace, G.G., Sassen, K., Wang, Z., Illingworth, A.J., O'Connor, E.J., Rossow,
1022 W.B., Durden, S.L., Miller, S.D., Austin, R.T., Benedetti, A., Mitrescu, C., and the CloudSat Science Team: The
1023 CloudSat mission and the A-Train: A new dimension and space-based observations of clouds and precipitation,
1024 *B. Am. Meteorol. Soc.*, 83, 1771-1790, <https://doi.org/10.1175/BAMS-83-12-1771>, 2002.

1025 Storer, R.L., Griffin, B.M., Hoft, J., Weber, J.K., Raut, E., Larson, V.E., Wang, M., and Rasch, P.J.: Parameterizing
1026 deep convection using the assumed probability density function method, *Geosci. Model Dev.*, 8, 1-19,
1027 <https://doi.org/10.5194/gmd-8-1-2015>, 2015.

1028 Strauss, D., and Paolino, D.: Intermediate time error growth and predictability: tropics versus mid-latitudes, *Tellus A:*
1029 *Dynamics and Meteorology and Oceanography*, 61, 579-586, <https://doi.org/10.1111/j.1600-0870.2009.00411.x>,
1030 2008.

1031 Suhas, E., and Zhang, Q.J.: Evaluation of trigger functions for convective parameterization schemes using
1032 observations, *J. Climate*, 27, 7647-7666, <https://doi.org/10.1175/JCLI-D-13-00718.1>, 2014.

1033 Taylor, K.E., Stouffer, R.J., and Meehl, G.A.: An overview of CMIP5 and the experiment design, *B. Am. Meteorol.*
1034 *Soc.*, 93, 485-4398, <https://doi.org/10.1175/BAMS-D-11-00094.1>, 2012.

1035 Thayer-Calder, K., Gettelman, A., Craig, C., Goldhaber, S., Bogenschutz, P.A., Chen, C.-C., Morrison, H., Höft, J.,
1036 Raut, E., Griffin, B.M., Weber, J.K., Larson, V.E., Wyant, M.C., M. Wang, Guo, Z., and Ghan, S.J.: A unified
1037 parameterization of clouds and turbulence using CLUBB and subcolumns in the Community Atmosphere Model,
1038 *Geosci. Model Dev.*, 8, 3801-3821, <https://doi.org/10.5194/gmd-8-3801-2015>, 2015.

1039 Thompson, G., Field, P.R., Rasmussen, R.M., and Hall, W.D.: Explicit forecasts of winter precipitation using an
1040 improved bulk cloud microphysics scheme. Part II: Implementation of a new snow parameterization, Mon.
1041 Weather Rev., 136, 5095-5115, <https://doi.org/10.1175/2008MWR2387.1>, 2008.

1042 Thompson, G., Rasmussen, R.M., and Manning, K.: Explicit forecasts of winter precipitation using an improved bulk
1043 cloud microphysics scheme. Part I: Description and sensitivity analysis, Mon. Weather Rev., 132, 519-542,
1044 [https://doi.org/10.1175/1520-0493\(2004\)132<0519:EFOWPU>2.0.CO;2](https://doi.org/10.1175/1520-0493(2004)132<0519:EFOWPU>2.0.CO;2), 2004.

1045 Thompson, G., Tewari, M., Ikeda, K., Tessoroff, S., Weeks, C., Otkin, J., and Kong, F.: Explicitly-coupled cloud
1046 physics and radiation parameterizations and subsequent evaluation in WRF high-resolution convective forecasts,
1047 Atmos. Res., 168, 92-104, <https://doi.org/10.1016/j.atmosres.2015.09.005>, 2016.

1048 Tokioka, T., Yamazaki, K., Kotoh, A., and Ose, T.: The equatorial 30-60 day oscillation and the Arakawa-Schubert
1049 penetrative cumulus parameterization, J. Meteor. Soc. Japan, 66, 883-900,
1050 https://doi.org/10.2151/jmsj1965.66.6_883, 1988.

1051 Waliser, D.E., Li, J.-L., Woods, C.P., Austin, R.T., Bacmeister, J., Chern, J., Del Genio, A., Jiang, J.H., Juang, Z.,
1052 Meng, H., Minnis, P., Platnick, S., Rossow, W.B., Stephens, G.L., Sun-Mack, S., Tao, W.-K., Tompkins, A.M.,
1053 Vane, D.G., Walker, C., and Wu, D.: Cloud ice: A climate model challenge with signs and expectations of
1054 progress, J. Geophys. Res., 114, D00A21, <https://doi.org/10.1029/2008JD010015>, 2009.

1055 Wicker, L.J., and W.C. Skamarock: Time-splitting methods for elastic models using forward time schemes, Mon.
1056 Weather Rev., 130, 2088-2097, [https://doi.org/10.1175/1520-0493\(2002\)130<2088:TSMFEM>2.0.CO;2](https://doi.org/10.1175/1520-0493(2002)130<2088:TSMFEM>2.0.CO;2), 2002.

1057 Wielicki, B.A., Barkstrom, B.R., Harrison, E.F., Lee III, R.B., Smith, G.L., and Cooper, J.E.: Clouds and the Earth's
1058 Radiation Energy System (CERES): An Earth Observing System experiment, B. Am. Meteorol. Soc., 77, 853-
1059 868, [https://doi.org/10.1175/1520-0477\(1996\)077<0853:CATERE>2.0.CO;2](https://doi.org/10.1175/1520-0477(1996)077<0853:CATERE>2.0.CO;2), 1996.

1060 Williamson, D.: The effect of time step and time-scales on parameterization suites. Quart. J. Roy. Meteor. Soc., 139,
1061 548-560, <https://doi.org/10.1002/qj.1992>, 2013.

1062 Wong, M., and Skamarock, W.C.: Spectral characteristics of convective-scale precipitation observations and forecasts,
1063 Mon. Weather Rev., 144, 4183-4195, <https://doi.org/10.1175/MWR-D-16-0183.1>, 2016.

1064 Xu, K.-M. and Krueger, S.K.: Evaluation of cloudiness parameterizations using a cumulus ensemble model, Mon.
1065 Weather Rev., 119, 342-367, [https://doi.org/10.1175/1520-0493\(1991\)119<0342:EOCPUA>2.0.CO;2](https://doi.org/10.1175/1520-0493(1991)119<0342:EOCPUA>2.0.CO;2), 1991.

1066 Xu, K.-M., and Randall, D. A.: A semi-empirical cloudiness parameterization for use in climate models, J. Atmos.
1067 Sci., 53, 3084-3102, [https://doi.org/10.1175/1520-0469\(1996\)053<3084:ASCPFU>2.0.CO;2](https://doi.org/10.1175/1520-0469(1996)053<3084:ASCPFU>2.0.CO;2), 1996.

1068 Zheng, Y., Alapaty, K., Herwehe, J. A., Del Genio, A.D., and Niyogi, D.: Improving high-resolution weather forecasts
1069 using the Weather Research and Forecasting (WRF) model with an updated Kain-Fritsch scheme, Mon. Weather
1070 Rev., 144, 833-860, <https://doi.org/10.1175/MWR-D-15-0005.1>, 2016.